(Received 2 June 2026, Accepted 23 June 2026, Scheduled 27 June 2026)

A Phase-Interrogated Surface Plasmon Resonance Sensor Based on a Graphene Oxide-Functionalized Ag/ZnSe Platform for Dopamine Detection

Faten Bashar Kamal Eddin[1], Jian Sun[2], Guanghui Chen[3], Maofa Zeng[4], Wenjun Jin[5], Houxin Fan[1], De-Man Han[2], and Sailing He[1, 2, *]

[1] *Centre for Optical and Electromagnetic Research, College of Optical Science and Engineering Zhejiang University, Hangzhou 310058, China*
[2] *Taizhou University, Jiaojiang 318000, China*
[3] *Zhejiang Hisun Pharmaceutical Co., Ltd., China*
[4] *Taizhou Institute for Food and Drug Control, Taizhou 318015, China*
[5] *Zhejiang Xianju Pharmaceutical Co., Ltd., Taizhou 317300, Zhejiang, China*

ABSTRACT: Dopamine (DA) is a critical neurotransmitter whose abnormal levels are associated with neurological disorders, including Parkinson's disease, Alzheimer's disease, and schizophrenia. The development of sensitive and reliable detection methods is therefore essential for diagnosis and treatment monitoring. Here we report a phase-interrogated surface plasmon resonance (SPR) biosensor based on a graphene oxide (GO)-functionalized glass/Ti/Ag/Al_2O_3/ZnSe multilayer platform. The high refractive index (RI) ZnSe layer confined the evanescent field through a waveguide-coupled mode, which produced a sharp resonance with a measured FWHM of 0.077°, a Q-factor of 799, and a figure of merit (FOM) of 1527 RIU^{-1}. The slight broadening relative to the simulated FWHM of 0.034° is consistent with practical fabrication imperfections and beam angular divergence, though sensor performance was not meaningfully affected. The bulk RI calibration with glucose solutions confirmed a phase sensitivity of 4.53×10^4 deg RIU^{-1} and an angular sensitivity of 120.1°/RIU. For DA detection, the ZnSe surface was functionalized with (3-aminopropyl)triethoxysilane (APTES) and GO and then exposed to different DA concentrations from 1 pM to 10 nM. A semi-log linear fit over the range of 1 pM to 1 nM showed a sensitivity of 1.15°/decade ($R^2 = 0.9547$), and a Langmuir isotherm yielded a maximum phase shift of 3.74°, a dissociation constant of 10 pM with R^2 of 0.9987. The limit of detection was 10 pM, and the signal-to-noise ratios (SNRs) ranged from 1.12 at 1 pM to 11.52 at 1 nM. The intra-chip coefficients of variation remained between 0.70% and 2.47%. Beyond clinical diagnostics, this platform holds promise for pharmaceutical applications, including drug development, pharmacokinetic/pharmacodynamic profiling, and therapeutic drug monitoring, where reliable small-molecule detection is increasingly required. This work, therefore, offers a straightforward, label-free route to picomolar DA detection with a clear path toward real-sample validation and selectivity assessment.

1. INTRODUCTION

Dopamine (DA) is a catecholamine neurotransmitter that plays essential roles in the central nervous, cardiovascular, renal, and hormonal systems. It governs movement, emotion, memory, motivation, and reward processing [1–4]. Abnormal levels of DA are strongly associated with several neurological and psychiatric disorders, including Parkinson's disease, Alzheimer's disease, schizophrenia, and depression. For instance, the progressive loss of dopaminergic neurons in the substantia nigra is a hallmark of Parkinson's disease, leading to characteristic motor symptoms. Consequently, the accurate and sensitive detection of DA in biological fluids has become a critical objective in clinical diagnostics, neurochemical research, and therapeutic monitoring [5–8]. There are numerous analytical techniques developed for DA determination, such as high-performance liquid chromatography [9, 10], fluorescence [11, 12], chemiluminescence [13], mass spectrometry [14], capillary electrophoresis [15], and electrochemistry [16].

From an industrial pharmaceutical perspective, the ability to monitor DA levels with high sensitivity and reliability is of growing interest not only in diagnostics but also in drug development and quality control. Dopaminergic dysfunction is a key target in the development of therapeutics for Parkinson's disease, schizophrenia, and depression. In drug discovery, precise measurement of DA and its metabolites in preclinical models and clinical trials is essential for pharmacokinetic/pharmacodynamic (PK/PD) profiling, dose optimization, and safety assessment. Furthermore, the increasing emphasis on personalized medicine and continuous therapeutic drug monitoring (TDM) demands analytical platforms that are not only highly sensitive and selective but also compatible with point-of-care or near-patient testing scenarios. The present work, which combines a high-performance phase-interrogation SPR sensor with a microfluidic format, directly addresses these

* Corresponding author: Sailing He (sailing@zju.edu.cn).

industrial needs by offering a label-free, rapid, and potentially scalable solution for DA detection.

To meet these diagnostic and industrial demands, surface plasmon resonance (SPR) biosensing has emerged as a particularly attractive platform. SPR enables direct, dynamic detection without exogenous labels and is readily compatible with microfluidic miniaturization, making it ideal for point-of-care and high-throughput applications [17–20]. In the Kretschmann configuration, a thin metal film (typically Au or Ag) is deposited on a glass prism. When P-polarized light is directed onto the metal film at an angle greater than the critical angle, it generates an evanescent field that couples to surface plasmon polaritons (SPPs) at the metal-dielectric interface. A sharp dip in the reflected intensity occurs when the wave vector of the incident light matches that of the SPPs. The resonance angle is exquisitely sensitive to the refractive index (RI) of the medium adjacent to the metal film, typically within ~ 200 nm of the interface. Hence, any molecular adsorption or binding event at the surface produces a measurable shift in the resonance angle (angular interrogation) or a change in the reflected intensity (intensity interrogation) [21, 22]. The field of plasmonic sensing has matured rapidly, evolving from fundamental light-matter interaction studies into a sophisticated discipline focused on integrated, high-performance diagnostics. Modern research has moved beyond traditional prism-based architectures, increasingly leveraging advanced nanophotonic designs to overcome physical constraints on sensitivity and resolution. Recent scholarly reviews demonstrate this paradigm shift: researchers are now employing Fano-resonant MIM waveguides to achieve ultrasharp transmission features [23] and utilizing photonic crystal fibers (PCF) to create flexible, miniaturized sensing platforms [24]. Beyond device architecture, significant effort is being directed toward the material science of sensing. The development of multifunctional plasmonic heterojunctions that integrate noble metals with semiconductors has proven essential for enhancing near-field amplification and enabling unlabelled, instantaneous detection in complex matrices [25]. These innovations are central to the emerging requirement for smart, distributed monitoring systems that must operate reliably in diverse, real-world conditions [26]. Ultimately, these collective advances from surface-enhanced Raman spectroscopy (SERS)-based pollutant mapping to plasmonic-enhanced water purification and desalination technologies are bridging the gap between theoretical nanophotonics and sustainable, scalable industrial applications [27, 28]. This technological landscape is further complemented by significant innovations in optical imaging and hyperspectral analysis. For instance, the longitudinal monitoring of angiogenesis in murine models has been demonstrated using noninvasive photoacoustic microscopy and optical coherence tomography [29]. Similarly, hyperspectral transmission microscopic imaging coupled with machine learning has been successfully implemented for the classification and identification of microalgae species and the estimation of their growth stages [30]. The utility of spectral feature extraction is further highlighted by the use of dual-mode microscopic hyperspectral imaging to achieve accurate classification of medicinal plant origins and varieties [31]. Beyond spectral analysis, longitudinal diagnostic capabilities have been advanced through the use of photoacoustic microscopy and optical coherence tomography to assess metastatic potential through longitudinal vasculature imaging of a biomaterial scaffold [32]. The development of multi-mode microscopic hyperspectral imagers has further expanded the applicability of these technologies across reflection and fluorescence detection modes [33]. These imaging advancements are supported by the development of a semi-anthropomorphic photoacoustic calcaneus phantom created via nano-CT and 3D printing, which provide a stable platform for calibrating bone-health sensing systems [34]. These imaging and waveguide-based advances are complemented by significant progress in complementary plasmonic sensing architectures, including photonic crystal fiber sensors, metasurface absorbers, and hybrid metal-graphene cavities. Chao et al. designed an SPR-photonic crystal fiber SPR-PCF temperature sensor employing an external Ag/SiO_2-coated trapezoidal-shaped surface with two layers of elliptical air-hole rings, achieving a maximum temperature sensitivity of 5200 pm/°C and a resolution of 0.01923°C through efficient coupling between the core-guided mode and surface plasmon-polariton modes [35]. In the terahertz regime, Sabaruddin et al. developed a five-band metasurface absorber based on gold cross-bar resonators atop a polyimide spacer and ground plane, achieving RI sensitivities up to 14 THz/RIU and FOMs as high as 140 RIU^{-1} across multiple resonant modes [36]. The same group further proposed a broadband terahertz absorber hybridizing gold and graphene metasurfaces separated by SiO_2 spacers, yielding a maximum absorptance of 98.9% with greater than 80% absorption over a 1.0 THz bandwidth through synergistic surface, cavity, and gap plasmon resonances [37]. In the visible-to-near-infrared range, Chau et al. reported a bidirectional bilayer-graphene metamaterial absorber with bowtie-shaped apertures, which produces nine ultra-narrowband Fano resonances (average $\sim$ 98% absorptance, quality factor (Q-factor) $\sim$ 215 under top illumination for hyperspectral sensing, while bottom illumination induces broadband absorption ($> 90\%$) for solar-thermal harvesting, with demonstrated sensitivity of 1306 nm/RIU and FOM of 261.21 RIU^{-1} [38].

Despite this rapid progress, conventional SPR suffers from two main drawbacks. First, the resonance dip in angular or intensity mode is relatively broad (full width at half maximum, FWHM, typically several degrees) due to plasmonic damping in the metal. This results in a low Q-factor and a modest figure of merit (FOM). Consequently, the sensitivity to small RI changes is limited. Second, phase-interrogated SPR, which measures the phase change of the reflected light upon resonance, offers much higher sensitivity because the phase undergoes a sharp jump at resonance. However, conventional phase-interrogation systems require interferometric setups, which are sensitive to mechanical vibrations and temperature fluctuations of the non-common paths in optical configurations. Moreover, they suffer from poor chip integration and high instrumentation cost [39–41]. A notable advance was reported by Liu et al. (2023), who overcame these challenges by using a SiO_2 waveguide on an Ag film. The waveguide couples the guided mode to the surface plasmon, directing the electromagnetic field towards the sensing interface and producing an exceptionally narrow resonance with FWHM of 0.2°. They extracted the phase without an in-

terferometer by simply rotating an analyzer in front of a CCD camera; the S-polarized component (which does not excite the SPR) served as an on-chip phase reference. The demodulated phase sensitivity reached 1.1×10^5 deg/RIU, and they successfully detected α-synuclein at a concentration of 300 pg/mL [42]. Graphene oxide (GO) has attracted enormous interest in biosensing due to its large surface area, excellent water dispersibility, and abundant oxygen-containing functional groups (carboxyl, hydroxyl, epoxy). These groups enable strong interactions with aromatic molecules such as DA through π-π stacking, hydrogen bonding, and electrostatic forces. Moreover, GO has a high RI and can be deposited as an ultra-thin film, making it an ideal platform for SPR signal amplification [43–45]. Several GO-based sensors for DA detection have been reported, predominantly employing electrochemical (EC) transduction. Gao et al. (2013) [46] prepared a GO-modified glassy carbon electrode (GO/GCE) using a covalent coupling method and found that the GO layer greatly enhanced the electrochemical response of DA while completely suppressing that of ascorbic acid (AA), achieving a linear range of 1.0–15.0 µM with an LOD of 0.27 µM. Yu et al. (2014) [47] fabricated a three-dimensional interpenetrating electrochemically reduced GO (ErGO) electrode that selectively detected DA in the presence of AA and uric acid (UA), with a linear range of 0.1–10 µM and a detection limit of 0.1 µM. Beyond bare GO, numerous composites have been developed to further enhance EC performance. For instance, Han et al. (2014) [48] prepared a covalently bonded GO-porphyrin composite (GO-P) by the condensation of GO with 5,15-pentafluorophenyl-10,20-p-aminophenylporphyrin, then electrochemically reduced it to ERGO-P for the simultaneous detection of DA and serotonin. The porphyrin moiety provided enhanced electrocatalytic activity toward neurotransmitter oxidation, achieving an LOD of 35 nM for DA with negligible interference from AA. A particularly sensitive approach was reported by Wang et al. (2015) [49], who developed an ultrasensitive and selective voltammetric aptasensor for DA based on a conducting polymer nanocomposite doped with GO and functionalized with an aptamer (poly(3,4-ethylenedioxythiophene)/rGO/aptamer) achieving an exceptionally low detection limit of 78 fM over a linear range of 1 pM–160 nM. Qian et al. (2014) [50] developed gold nanoparticles decorated polypyrrole (PPy)/rGO hybrid sheets that achieved a detection limit of 18.29 pM over a linear range of 0.1–5000 nM, demonstrating the synergistic effect of metal nanoparticles and conducting polymers on graphene scaffolds. These works illustrate that GO and its derivatives, when combined with metal nanoparticles, conducting polymers or aptamers, can deliver remarkable EC performance for DA detection. Kamal Eddin et al. (2023) [51] developed a GO-based SPR sensor that showed a sensitivity of 0.2148°/pM and LOD of 0.1 pM, with a response time of 5 min. The sensor exhibited good selectivity in the presence of epinephrine, AA and UA, attributing this preference to the primary amine group of DA as opposed to the methylated secondary amine of epinephrine. However, this sensor operated with an extremely low signal-to-noise ratio (SNR), a direct consequence of the broad resonance dips inherent to angular-interrogated SPR. The FWHM of the SPR reflectivity curves increased from 3.04° for the bare GO film to 3.40° at 1 nM DA, causing the detection accuracy to decrease and the FOM to drop by nearly 10% across the concentration range. This fundamental limitation of angular SPR, the trade-off between sensitivity enhancement and dip broadening when adding functional layers, means that although femtomolar LODs can be achieved through calibration curve fitting, the reliability of individual measurements at trace concentrations remains compromised. Moreover, the immobilization of GO on sensor surfaces often employs (3-aminopropyl)triethoxysilane (APTES) as a linker, as demonstrated by Zhang et al. (2016) [43] for microfluidic exosome capture, where APTES was used to silanize the surface before GO adsorption. The silanization process creates a stable amine-terminated monolayer that can form covalent or electrostatic bonds with the carboxyl groups of GO, yielding a robust, uniform coating that withstands aqueous flow conditions. This simple and robust method is directly applicable to our SPR chip and offers advantages over physical adsorption in terms of layer stability and reproducibility. Zinc selenide (ZnSe) is a II-VI semiconductor with a high RI and low optical absorption in the visible range. When deposited as a thin film on an Ag layer, ZnSe can significantly enhance the evanescent field at the metal-dielectric interface, increasing the spatial overlap between the plasmonic field and the sensing layer. This property has been exploited in several SPR sensors for biomolecule detection.

To the best of our knowledge, a phase-interrogated SPR biosensor that combines a GO-functionalized ZnSe/Ag multilayer architecture has not been reported. Such a configuration could exploit the high Q-factor and phase sensitivity demonstrated by Liu et al. [42], while benefiting from the superior surface chemistry and field confinement provided by ZnSe and GO. We therefore developed a phase-interrogated SPR sensor based on a glass/Ti(1 nm)/Ag(48 nm)/Al_2O_3(1 nm)/ZnSe(115 nm) multilayer. The Ti adhesion layer and thin Al_2O_3 capping layer were included to ensure structural integrity and prevent Ag oxidation, respectively. The ZnSe layer was chosen for its high RI to enhance the evanescent field. The sensor's bulk RI response was first characterized by using glucose solutions to establish the phase sensitivity and linear dynamic range. The ZnSe surface was subsequently functionalized with APTES, followed by GO immobilization, to create a high-surface-area recognition interface for DA. The functionalized sensor was then applied to the detection of DA over a concentration range from 1 pM to 10 nM. The binding characteristics were analyzed using semi-log linear calibration and Langmuir isotherm models. The intra-chip reproducibility was assessed through replicate measurements.

2. MATERIALS AND METHODS

2.1. Reagents and Chemicals

Hydrogen peroxide, acetone, isopropanol, sulfuric acid AZ5214 photoresist, RZX-3080 developer, polydimethylsiloxane (PDMS, DOWSIL DC184), RI matching liquid ($n = 1.52$), DA hydrochloride, and absolute ethanol were

used as received without further purification. A pair of 45° right-angle N-BK7 prisms (model OQRPB25.4, 25.4 mm) and K9 glass substrates were obtained from Beijing Maofeng Optoelectronics Technology Co., Ltd. (Beijing, China). D-(+)-Glucose (≥ 99.5%, CAS 50-99-7, MW 180.16 g/mol; Sigma-Aldrich) was dissolved in deionized water to prepare standard solutions for evaluating the intrinsic sensing performance of the bare chip. Single-polished silicon wafers, SU8-2015 negative photoresist, and propylene glycol methyl ether acetate (PGMEA) developer were employed for microfluidic mold fabrication. Phosphate-buffered saline (PBS, pH 7.2–7.4, 0.01 M; catalog P1020-500 mL) was purchased from Solarbio, supplied via Hangzhou Youke Biotechnology Co., Ltd. (3-Aminopropyl)triethoxysilane (APTES, ≥ 98%, CAS 919-30-2, MW 221.37 g/mol; Sigma-Aldrich) served as the silane coupling agent for amine functionalization of the ZnSe sensing surface. GO gel (Aladdin, catalog no. G139812, CAS 7782-42-5) was dispersed in deionized water at 0.5 mg/mL to form the GO functional layer.

2.2. Theoretical Simulations

The transfer matrix method (TMM) provides a well-established analytical framework for modeling how electromagnetic waves propagate through layered planar structures. In this work, TMM was used to simulate the optical response of the multilayer SPR sensing stack. Each individual layer is described by a 2×2 characteristic matrix that encodes both the phase accumulated during propagation and the boundary conditions at the layer interfaces. For P-polarized (TM) illumination, the characteristic matrix of the ith layer is given by [52–54]:

$$M^{(i)} = \begin{pmatrix} M^{(i)}_{(1,1)} & M^{(i)}_{(1,2)} \\ M^{(i)}_{(2,1)} & M^{(i)}_{(2,2)} \end{pmatrix} = \begin{pmatrix} \cos\left(p^{(i)}\right) & -i\frac{\sin\left(p^{(i)}\right)}{q^{(i)}} \\ -iq^{(i)}\sin\left(p^{(i)}\right) & \cos\left(p^{(i)}\right) \end{pmatrix} \quad (1)$$

where the propagation phase and the optical admittance of layer i are respectively defined as:

$$p^{(i)} = k_0 d^{(i)} \sqrt{n^{(i)^2} - n^{(1)^2}\sin^2\theta} \quad (2)$$

$$q^{(i)} = \frac{1}{n^{(i)^2}} \sqrt{n^{(i)^2} - n^{(1)^2}\sin^2\theta} \quad (3)$$

Here, $k_0 = 2\pi/\lambda$ is the free-space wavenumber; $d^{(i)}$ is the thickness of the ith layer; $n^{(1)}$ and $n^{(i)}$ are the complex refractive indices of the incident medium (prism) and the ith layer respectively; and θ is the angle of incidence measured from the surface normal.

The total transfer matrix of the full multilayer stack comprising the prism, Ti adhesion layer, Ag plasmonic film, Al_2O_3 spacer, and ZnSe sensing layer is obtained by multiplying the individual layer matrices in sequence:

$$M_{total} = \prod_i M^{(i)} \quad (4)$$

The complex Fresnel reflection coefficient of the complete stack is then computed as:

$$\tilde{r} = \frac{q^1\left(M_{total(1,1)} + q^{(N)}M_{total(1,2)}\right) - \left(M_{total(2,1)} + q^{(N)}M_{total(2,2)}\right)}{q^1\left(M_{total(1,1)} + q^{(N)}M_{total(1,2)}\right) + \left(M_{total(2,1)} + q^{(N)}M_{total(2,2)}\right)} \quad (5)$$

where $q^{(1)}$ and $q^{(N)}$ are the optical admittances of the prism and sensing medium, respectively. The reflectance and reflected phase are then recovered directly as:

$$R = |r|^2, \quad \varphi = \arg(\tilde{r}) \quad (6)$$

SPR coupling arises because the in-plane photon momentum in free space always falls short of the surface plasmon polariton (SPP) dispersion curve. In the Kretschmann configuration, a prism is used to overcome this momentum mismatch. When light undergoes total internal reflection at the base of the prism, the in-plane component of its wave vector is boosted sufficiently to match that of the SPPs, allowing resonant excitation to occur at a well-defined angle of incidence [55–57]. Using the TMM framework, the thicknesses and refractive indices of each layer, including the ZnSe sensing surface, were iteratively optimized to minimize the FWHM and maximize the phase sensitivity $\partial\varphi/\partial n$ at the operating wavelength of 632.8 nm. To simulate the near-field electric field distribution across the multilayer stack as well as the base Ag-based structure, COMSOL Multiphysics (v6.2) was employed at $\lambda = 632.8$ nm, with each layer assigned its experimentally determined complex RI and TMM-optimized thickness, and perfectly matched layer (PML) boundary conditions applied at all domain boundaries.

2.3. Fabrication of Microfluidic and Sensor Chip

The microfluidic slab was constructed through a PDMS replica molding approach (Figure 1(a)). To prepare the silicon mold, we diced a 4-inch single-polished silicon wafer into 30 mm × 30 mm segments, then cleaned the pieces with piranha (sulfuric acid : hydrogen peroxide = 7 : 3) to eliminate organic contaminants. This was followed by ultrasonic washing in acetone and isopropanol, and blow-drying with nitrogen. The negative photoresist SU8-2015 was applied by spin coating, thermally treated at 65°C and subsequently 95°C during pre-baking, and then patterned via mask-based UV exposure (SUSS MicroTec MA6, 350 W) under soft-contact mode for 45 s. Following that,

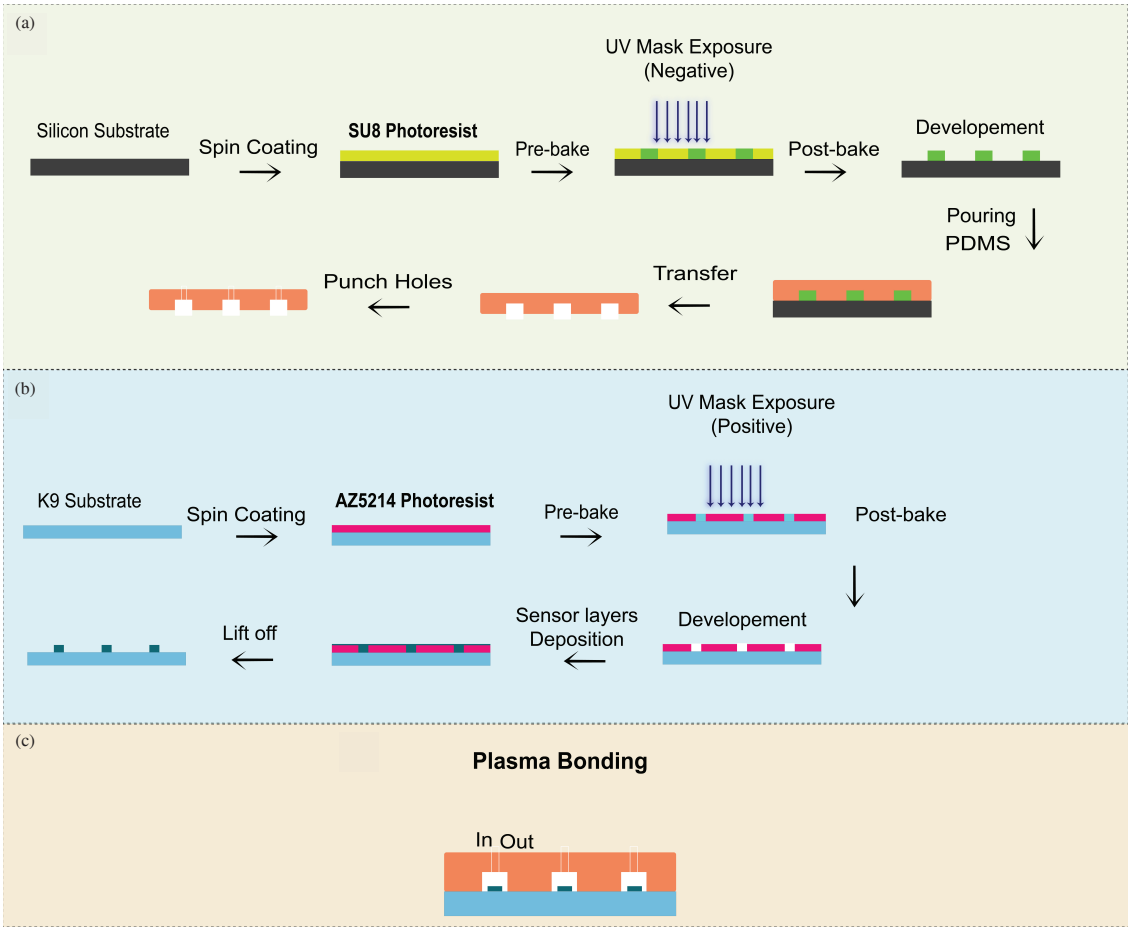

FIGURE 1. Schematic illustration of the fabrication and integration of the SPR sensor chip with the PDMS microfluidic channels. (a) Fabrication of the PDMS microfluidic channel using UV lithography with a customized mask on a silicon wafer coated with SU-8 photoresist. (b) Preparation of the SPR sensor chip on a K9 glass substrate through UV lithography using AZ5214 photoresist, followed by electron beam evaporation of the Ti/Ag/Al_2O_3/ZnSe layers with subsequent lift-off processing. (c) Plasma bonding of the PDMS microchannel onto the SPR sensor chip.

the exposed resist was developed in PGMEA and then cleaned with isopropanol, producing a silicon mold bearing ten channel structures. PDMS (DOWSIL, DC184) was prepared by mixing the base and curing agent at a 10 : 1 weight ratio, placing the mixture under vacuum for roughly 30 minutes to eliminate air bubbles, casting it over the mold, and allowing it to crosslink for 1 hour at 85°C. After that, we peeled off the cured PDMS and punched inlet/outlet holes at each channel end.

The fabrication sequence for the sensor chip is depicted in Figure 1(b). K9 glass substrates underwent the same piranha cleaning protocol, ultrasonic rinsing in acetone and isopropanol, and nitrogen drying. AZ5214 photoresist was spin-coated and baked at 95°C for 5 minutes. Lithographic patterning was performed in soft contact mode for 12 s using a mask aligner, after which the substrates received a post-exposure bake at 120°C for 2 minutes and a subsequent flood exposure of 24 s. The development of RZX-3080 solution and rinsing with deionized water defined ten isolated sensing regions on each substrate. A multilayer thin-film stack consisting of Ti (1 nm), Ag (48 nm), Al_2O_3 (1 nm), and ZnSe (115 nm) was deposited in sequence via electron beam evaporation (Denton, Explorer). The photoresist and overlying metal were removed by immersing the substrates in acetone under ultrasonic agitation, leaving behind ten well-defined sensing pads. The relevant optical constants at 632.8 nm are as follows: Ag $n = 0.056253 + 4.2760i$, Ti $n = 2.7039 + 3.7651i$, ZnSe $n = 2.5782$, and Al_2O_3 $n = 1.7663$. The PDMS microfluidic slab and the chips were subsequently bonded to each other through oxygen plasma activation (Harrick Plasma, PDC-002), as illustrated in Figure 1(c).

To evaluate the baseline sensing performance of the bare ZnSe surface, an initial SPR chip was tested without any surface functionalization. Glucose standard solutions at concentrations of 0, 0.5, 1, 1.5, 2, 2.5, 3, 3.5, 4, 4.5, 5, 5.5, 6, 6.5, and 7 mM were prepared in deionized water and sequentially injected into the microfluidic channels directly over the unmodified ZnSe sensing surface. This experiment served to characterize the intrinsic RI sensitivity of the sensor chip prior to any chemical modification, establishing a performance baseline for subsequent functionalized measurements. For DA detection, a separate set of sensor chips was prepared and functionalized through a layer-by-layer surface modification process. Surface functionalization of the ZnSe sensing area exposed within each channel was carried out as follows. An APTES solution at 5% (v/v) in absolute ethanol was introduced into the chan-

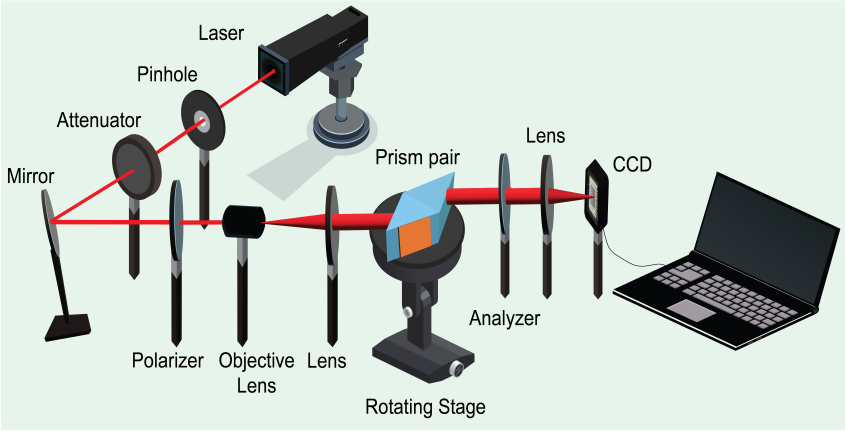

FIGURE 2. Schematic of the phase-interrogation SPR optical setup integrated with imaging. The SPR chip is integrated into the platform for phase extraction and time-resolved detection of glucose and DA.

nels and left to react for 1 hour at room temperature, generating a uniform amine-terminated monolayer on the ZnSe surface. The excess and unreacted silane molecules were flushed out by rinsing with deionized water. A GO suspension was then introduced into the functionalized channels. The adsorption of GO onto the APTES layer proceeded spontaneously through electrostatic attraction between the negatively charged oxygen-bearing groups on the GO sheets and the positively charged protonated amine groups of the silane. Following the incubation period, loosely bound GO was removed by rinsing with deionized water, completing the preparation of a GO-coated sensing surface capable of capturing DA molecules. For non-specific binding control experiments, two additional surface configurations were prepared on separate sensor chips following the same fabrication and functionalization protocols: (i) bare ZnSe surfaces (no functionalization) and (ii) APTES-only surfaces (silanized but without GO adsorption). These control surfaces were tested under identical flow and incubation conditions using a 1 nM DA solution, representing the highest concentration in the calibration series, to evaluate any non-specific phase response arising from the substrate or the linker layer. Prior to sensing measurements, DA standard solutions spanning concentrations from 1 pM to 10 nM were prepared by serial dilution in PBS (pH 7.4). The solutions were introduced sequentially into independent microfluidic channels, one concentration per channel, and permitted to interact with the sensing surface for 10 minutes at room temperature. This incubation period was selected to ensure sufficient time for binding equilibrium to be approached, based on the kinetic parameters established in our previous work, where adsorption rates of 0.391–1.138 min^{-1} were observed. Measurements performed 5 minutes after the injection were sufficient for complete interaction between DA and the GO film [51]. The slightly extended incubation time adopted here provides a conservative margin to account for the different sensor geometries and phase-interrogation readouts, ensuring that the measured phase shifts reflect stable binding rather than kinetic artifacts. Prior to each DA injection, a pure buffer baseline was recorded as a reference signal. The phase shifts induced by DA binding were monitored continuously using the phase-interrogation SPR system. Each DA concentration was introduced into a separate, dedicated microfluidic channel to prevent cross-contamination between concentrations, and no channel was used for multiple concentrations. Following that, a separate experiment was performed using a single GO-functionalized channel for Langmuir binding analysis. DA solutions at 1 pM to 10 nM were injected sequentially into the same channel without surface regeneration between concentrations, as standard acidic/alkaline regeneration protocols are incompatible with the GO/APTES/ZnSe surface chemistry. Between successive DA concentration injections, the channel was flushed with PBS buffer for 5 minutes to remove any unbound or weakly adsorbed molecules and to reestablish a stable baseline signal prior to the next injection. Each DA concentration was allowed to interact with the sensing surface for 10 minutes at room temperature.

2.4. Custom Optical Setup and Phase Extraction

The custom-built SPR system is illustrated in Figure 2. A 632.8 nm He-Ne laser served as the light source, with the output beam first passing through a pinhole spatial filter and an adjustable attenuator to clean and control the beam intensity. The beam was then redirected by a mirror, linearly polarized, and expanded through a combination of a 40× microscope objective and a collimating shaping lens to illuminate the full sensing area uniformly. To couple the expanded beam to the sensor chip, we used two N-BK7 prisms mounted on a rotating stage, allowing continuous adjustment of the incidence angle without disturbing other optical components. In this pair-prism geometry, the beam undergoes two total internal reflections at the parallel prism surfaces and emerges parallel to the incident beam. As a result, the reflected beam direction stays fixed during the angular scan, so the resonant coupling condition can be identified in real time through the CCD image as the gray value reaches its minimum, without any need to reposition downstream components. To extract the phase, we employed the phase-polarization modulation scheme proposed by Liu et al. (2023). A linear analyzer was rotated in equal steps of 20° over the range of 0° to 180°. The reflected intensity distribution across the sensing area was recorded at each analyzer position

by a CCD camera through an imaging lens. The modulation of the analyzer angle produces a sinusoidal variation in the CCD image's grayscale, described by [42]:

$$I = \gamma\left[1 + \alpha\cos\left(2A\right) + \beta\sin\left(2A\right)\right] \tag{7}$$

where A is the analyzer angle; α, β, and γ are the fitting coefficients for the sinusoidal modulation; and $\gamma = \left(I_P + I_S\right)/2$ encodes the total reflected intensity. The phase retardation Δ, defined as the phase difference between the P- and S-polarized components of the reflected light, is then recovered from the fitting coefficients as:

$$\cos\Delta = \frac{\beta}{\sqrt{1-\alpha^2}} \tag{8}$$

S-polarized light does not participate in SPR excitation because its electric field oscillates parallel to the interface and therefore cannot drive the transverse magnetic plasmon mode at the ZnSe sensing surface. As a result, the S-polarized component accumulates no additional phase shift upon reflection, making it an inherently stable reference signal throughout the measurement. Since both P- and S-polarized components travel along a completely shared optical path, this configuration acts as a common-path interferometer, entirely eliminating the need for external beam-splitting optics or a separate reference arm. For RI calibration of the sensor, glucose solutions of varying concentrations were used to establish the phase-to-RI response of the ZnSe-coated sensor chip.

3. RESULTS

3.1. Simulation and Theoretical Analysis

TMM simulations were first carried out for the proposed glass/Ti(1 nm)/Ag(48 nm)/Al_2O_3(1 nm)/ZnSe multilayer stack, and the results were benchmarked against conventional Au-only and Ag-only SPR configurations, both with a metal thickness of 48 nm. As shown in Figure 3(a), the bare Au and Ag films produced the characteristically broad and shallow resonance dips associated with the high plasmonic losses of flat metal films, whereas the proposed Ag/Al_2O_3/ZnSe structure yielded a significantly narrower and deeper dip, far better suited for high-sensitivity phase interrogation. This contrast is further reflected in Figure 3(b), where the phase responses of Au and Ag rose gradually and continuously with RI, while the Ag/Al_2O_3/ZnSe structure remained nearly flat before undergoing an abrupt near-vertical jump at the waveguide-coupled resonance condition. This sharp phase transition is a direct consequence of the narrow resonance linewidth and the high Q-factor achieved by the multilayer configuration, arising from the waveguide-like field confinement introduced by the ZnSe layer. To identify the optimal ZnSe thickness, the simulations were performed by systematically sweeping the ZnSe layer thickness from 114 to 150 nm while keeping the Ti (1 nm), Ag (48 nm), and Al_2O_3(1 nm) thicknesses fixed. As illustrated in Figure 3(c), increasing the ZnSe thickness progressively shifted the resonance dip toward higher incidence angles, while the dips simultaneously became shallower and broader. The corresponding phase responses in Figure 3(d) show a gradual flattening of the phase jump as the ZnSe thickness increased beyond the optimum, indicating that excessive field confinement within the ZnSe layer weakens the coupling strength between the guided mode and the surface plasmon. Conversely, reducing the ZnSe thickness below the optimum degraded both the resonance depth and the phase sensitivity, reflecting insufficient mode confinement and poor plasmon coupling. Based on these simulation results, a ZnSe thickness of 115 nm was selected as the optimum. Under these conditions, the TMM simulation yielded a resonance angle of 61.53°, an FWHM of 0.034°, and a Q-factor of 1837, confirming the strong potential of this structure for high-sensitivity phase-interrogation SPR sensing. To elucidate the physical origin of the enhanced phase sensitivity, COMSOL Multiphysics near-field simulations were performed at $\lambda = 632.8$ nm for both the conventional Glass/Ti/Ag structure and the optimized Glass/Ti/Ag/Al_2O_3/ZnSe configuration. The simulated electric field distributions are presented in Figures 3(e) and 3(f), respectively. In the conventional Ag SPR structure (Figure 3(e)), the normalized electric field $|E/E_0|$ was tightly confined to the immediate Ag-dielectric interface and decays rapidly and exponentially into the sensing medium, with an effective evanescent penetration depth of approximately 150 nm and less than 5% of the total field energy overlapping with the analyte volume. In contrast, the optimized ZnSe-coupled structure (Figure 3(f)) exhibited a fundamentally different field profile. The ZnSe layer ($n = 2.5782$), sandwiched between the Al_2O_3 barrier ($n = 1.7663$) and the aqueous sensing medium ($n = 1.333$), acts as a high-index dielectric waveguide. At a thickness of 115 nm, corresponding to the critical coupling condition between the Ag plasmonic mode and ZnSe guided mode, the propagation wavevector within ZnSe is real, confirming guided-mode confinement. The resulting $|E/E_0|$ values reach $\sim$ 14 at the ZnSe/water interface, with the field maintained at $\sim$ 8–10 throughout the ZnSe film thickness. In contrast, the conventional Ag SPR configuration exhibited a tightly confined evanescent field that decayed exponentially to negligible values within $\sim$ 50 nm, providing minimal spatial overlap with the sensing medium. The waveguide-coupled architecture therefore delivers a dramatically extended field distribution that maintains high intensity across the entire 115 nm ZnSe layer and into the aqueous medium, yielding a $\sim$ 10-fold improvement in field overlap with the sensing volume. The intensity enhancement factor ($|E|^2$) at the ZnSe/water interface is $\sim 9.8\times$ compared to the field at an equivalent distance in conventional Ag SPR, the field enhancement factor is $\sim 3.1\times$ in magnitude, and the effective penetration depth extends to $\sim$ 180–200 nm due to the gradual leakage of the guided mode. The field overlap integral analysis reveals that most of the field energy resides within the ZnSe layer and extends significantly into the water sensing region, yielding substantially improved overlap with the sensing volume compared to conventional Ag SPR. This waveguide-plasmon coupling produces a Fano-like resonance characterized by a dramatically narrowed FWHM of 0.034° compared to $\sim 1.2°$ for conventional Ag SPR; this $\sim$ 35-fold reduction in FWHM directly underpins the superior phase sensitivity of the present platform. The 115 nm ZnSe thickness

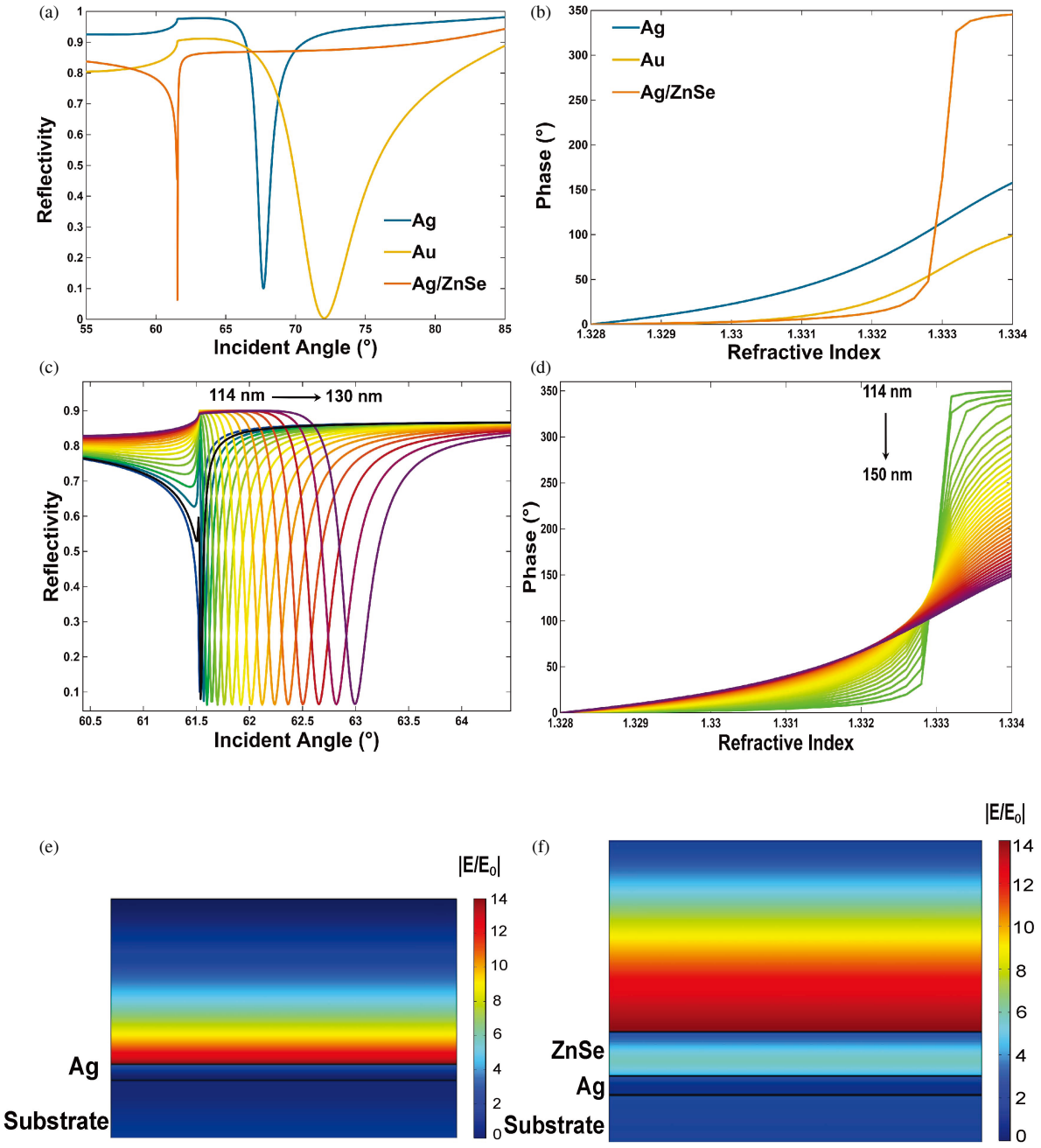

FIGURE 3. Theoretical analysis and simulation of waveguide-coupled SPR for the Ag/ZnSe structure. (a) Resonant angular spectra of conventional SPR (Au and Ag) versus the proposed Ag/Al_2O_3/ZnSe structure, (b) resonant phase versus RI for all three structures, (c) angular spectra with increasing ZnSe thickness (114–130 nm, left to right), (d) phase response versus RI for each ZnSe thickness (114–150 nm, top to bottom), (e) mode field distribution of the Glass/Ti/Ag structure, and (f) mode field distribution of the full Glass/Ti/Ag/Al_2O_3/ZnSe structure.

corresponds to the critical coupling condition where the SPR mode at the Ag surface and the guided mode within ZnSe are phase-matched, maximizing their mutual coupling and yielding the sharpest resonance and maximum phase sensitivity.

3.2. Experimental Optical Characterization and Phase Sensitivity

The fabricated sensor was first characterized in deionized water to establish the baseline resonance condition. The measured resonance angle was 61.52°, in excellent agreement with the TMM-predicted value of 61.53°, confirming that the fabricated glass/Ti(1 nm)/Ag(48 nm)/Al_2O_3(1 nm)/ZnSe(115 nm) stack faithfully reproduced the designed waveguide-coupled resonance. The incident angle was subsequently fixed at this value for all phase measurements, and the analyzer angle was rotated stepwise to modulate the polarization state of the reflected light, from which the differential phase between the P- and S-polarized components was extracted. The measured FWHM was 0.077°, yielding a Q-factor of 799. To evaluate the

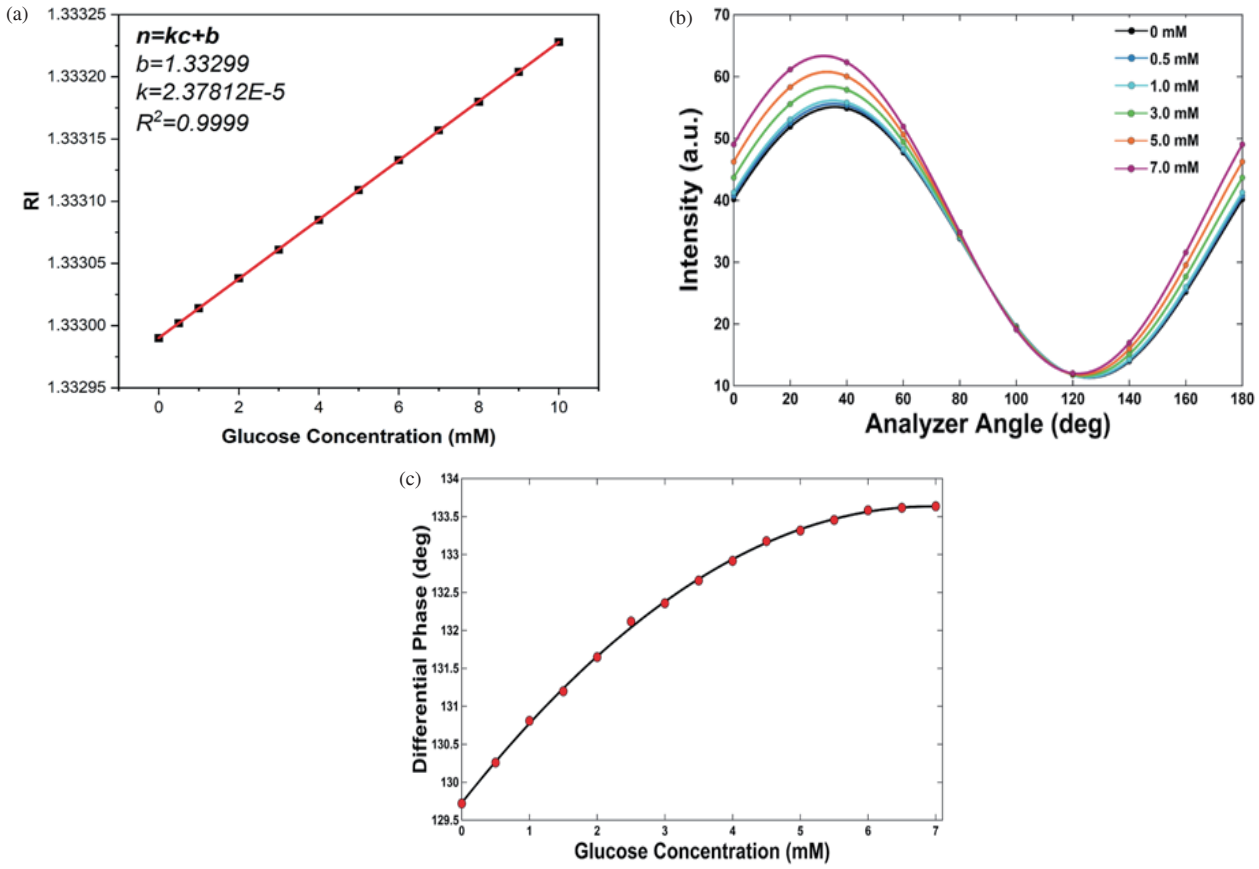

FIGURE 4. (a) Calibration curve showing the linear relationship between the RI and glucose concentration, (b) phase-polarization modulation for glucose solutions of varying concentrations, and (c) differential phase response as a function of glucose concentration.

phase sensitivity of the sensor, glucose solutions at concentrations ranging from 0 to 7 mM were prepared by serial dilution in deionized water. The baseline differential phase recorded in deionized water (0 mM) was 129.721°.

After that, each glucose solution was sequentially injected into the microfluidic channels over the bare ZnSe surface, and the incident angle was set to the resonance condition by locating the minimum grayscale intensity in the CCD image. The RI of each solution was determined by using the linear calibration relation $n = 2.37812 \times 10^5 c + 1.33299 (R^2 = 0.9999)$, established from the glucose-water RI increment $dn/dc = 2.38 \times 10^{-5}$ RIU/mM at 632.8 nm reported in the CRC Handbook of Chemistry and Physics [58], as shown in Figure 4(a). The analyzer was then rotated from 0° to 180° in steps of 20° to perform phase-polarization modulation, and the resulting sinusoidal intensity curves were fitted to extract the differential phase at each concentration, as shown in Figure 4(b). A phase shift of approximately 0.108° was observed at 0.1 mM glucose; however, this value approached the system noise floor and could not be considered a reliable measurement. As glucose concentration increased, the differential phase rose steadily, reaching 130.260° at 0.5 mM, 130.810° at 1 mM, 131.199° at 1.5 mM, 131.649° at 2 mM, 132.118° at 2.5 mM, 132.358° at 3 mM, 132.657° at 3.5 mM, 132.917° at 4 mM, 133.177° at 4.5 mM, 133.316° at 5 mM, 133.456° at 5.5 mM, 133.583° at 6 mM, 133.616° at 6.5 mM, and 133.636° at 7 mM. The corresponding phase shifts relative to the water baseline were 0.539°, 1.089°, 1.478°, 1.928°, 2.397°, 2.637°, 2.936°, 3.196°, 3.456°, 3.595°, 3.735°, 3.862°, 3.895°, and 3.915° respectively, as illustrated in Figure 4(c). Consequently, 0.5 mM was established as the practical lower detection limit of the sensor for bulk RI changes. At this concentration, the measured phase shift of 0.539° corresponded to an RI change of $\Delta n = 1.19 \times 10^{-5}$ RIU, yielding a phase sensitivity of 4.53×10^4 deg/RIU. This value reflects the steep phase jump characteristic of the waveguide-coupled resonance supported by the ZnSe layer, and highlights the sensor's strength in phase interrogation mode. The obtained sensitivity is governed by the specific multilayer configuration and resonance conditions, where the waveguide material, thickness, intermediate Al_2O_3 layer, and excitation wavelength collectively determine the guided-mode/plasmon coupling behavior. The ultrathin Al_2O_3 layer improves Ag stability against oxidation while slightly modifying the metal-dielectric interface. At 7 mM glucose, the sensor produced an angular shift of 0.02° with a negligible FWHM broadening of 0.005° (from 0.077° to 0.082°), confirming resonance stability under aqueous conditions, for an RI change of 1.67×10^{-4} RIU, corresponding to an angular sensitivity of 120.1°/RIU and a FOM of 1527 RIU^{-1}. It is worth noting that the phase sensitivity decreases progressively at higher concentrations, reaching approximately 2.34×10^4 deg/RIU at 7 mM, due to the inherently nonlinear

phase response beyond the steepest region of the resonance curve. The value reported at 0.5 mM therefore represents the maximum achievable phase sensitivity of the sensor under the present operating conditions.

The response was steepest at low concentrations and gradually flattened beyond approximately 4 mM, consistent with an increasing mismatch between the fixed incident angle and the shifting resonance condition at higher refractive indices. The observed decrease in phase sensitivity at higher glucose concentrations arises from the inherent nonlinearity of the phase response curve near the waveguide-coupled resonance condition. As shown in Figure 3(d), the phase shift exhibits a steep, nearly vertical jump within a very narrow angular range around the resonance angle; once the bulk RI change shifts the resonance condition away from this steepest region, the phase response becomes progressively flattened. This behavior is not a flaw of the sensor design but rather an intrinsic characteristic of phase-interrogation SPR, where the sensitivity is maximized only when the operating angle is precisely locked to the inflection point of the phase curve. At higher analyte concentrations, the RI change becomes sufficiently large to move the system out of this optimal region, causing the phase sensitivity to decline. To mitigate this limitation and extend the practical dynamic range, one straightforward strategy is to implement angle-phase dual-parameter interrogation: the resonance angle can be tracked for coarse quantification at high concentrations, while the phase response is reserved for high-sensitivity measurements at low concentrations. Alternatively, the incident angle could be actively re-optimized for each concentration range through a feedback-controlled rotation stage, ensuring that the system always operates at the steepest phase slope. These approaches are technically feasible with the current optical setup and would allow the sensor to maintain high sensitivity across a broader concentration spectrum without compromising its performance at trace levels.

3.3. DA Detection

Following the bulk RI characterization, a separate set of sensor chips was functionalized with APTES and GO for DA detection. The surface chemistry followed a two-step modification protocol adapted from the microfluidic functionalization approach reported by Zhang et al. [43], in which APTES silanization of the substrate was first performed to generate a stable amine-terminated monolayer, followed by electrostatic adsorption of the GO layer onto the protonated amine groups. In the present work, this same strategy was applied to the ZnSe sensing surface within the PDMS microfluidic channels. The APTES layer served dual purposes: it provided the chemical anchor for GO deposition through electrostatic attraction between the positively charged amine groups and the negatively charged oxygen-containing groups of GO, and it ensured a robust and uniform coating that withstands aqueous flow conditions. The GO layer in turn provided the active capture surface for DA, exploiting the well-established interactions between GO and DA through π-π stacking, hydrogen bonding, and electrostatic forces arising from its abundant carboxyl, hydroxyl, and epoxy functional groups. This simple yet robust two-layer functionalization approach is directly compatible with microfluidic integration and offers reproducible surface coverage without the need for covalent coupling chemistry. Prior to DA injection, a PBS baseline was established, yielding a differential phase of 143.487°. DA standard solutions at concentrations of 1, 10, 100, 1000, and 10000 pM were then sequentially injected into the GO-functionalized microfluidic channels and allowed to interact with the sensing surface for 10 minutes at room temperature. The differential phase increased progressively with DA concentration, rising from 143.851° at 1 pM to 145.362° at 10 pM, 146.769° at 100 pM, 147.223° at 1 nM, and 147.607° at 10 nM, corresponding to phase shifts of 0.364°, 1.875°, 3.282°, 3.736°, and 4.120° relative to the PBS baseline, respectively. To confirm that the measured phase response originates from specific DA-GO interactions rather than non-specific adsorption, control experiments were conducted by injecting 1 nM DA over bare ZnSe and APTES-only functionalized surfaces under identical flow conditions. The bare ZnSe surface produced a baseline differential phase of 113.823° in PBS, which shifted by less than 0.02° upon injection of 1 nM DA (from 113.823° to 113.844°), well within the system noise floor (SNR <1). The APTES-only functionalized surface produced a baseline differential phase of 120.701° in PBS, which shifted by less than 0.05° upon injection of 1 nM DA (from 120.701° to 120.748°), also within the system noise floor. In contrast, the fully GO-functionalized surface produced a phase shift of 3.736° at 1 nM DA (from 143.487° to 147.223°), corresponding to a specific-to-non-specific signal ratio exceeding 70-fold at the highest tested concentration. These results confirm that neither the ZnSe substrate nor the APTES linker layer contributes meaningfully to the sensing signal and that the phase response reported subsequently is attributable exclusively to specific molecular recognition at the GO capture layer rather than to non-specific physisorption at the underlying substrate. In the concentration range 1 pM to 1 nM, the phase response followed a semi-log linear trend with a sensitivity of 1.15°/decade ($R^2 = 0.9547$), as shown in Figure 5(a), covering the physiologically relevant concentration window for DA detection in biological fluids. Subsequently, a separate experiment was performed using a single GO-functionalized channel. DA solutions at 1 pM, 10 pM, 100 pM, 1 nM, and 10 nM were injected sequentially into the same channel. Between Between successive DA concentration injections, the channel was flushed with PBS buffer for 5 minutes to remove unbound and weakly adsorbed molecules, ensuring that the recorded phase shift at each step reflects only the specifically bound DA fraction rather than a physisorbed background. The PBS baseline yielded a differential phase of 128.294°. Upon sequential DA injection, the differential phase increased to 128.660° at 1 pM, 130.226° at 10 pM, 131.628° at 100 pM, 132.075° at 1 nM, and 132.676° at 10 nM, corresponding to a total cumulative phase shift of 4.382° relative to the PBS baseline. Fitting the single-channel data over the 1 pM–1 nM range to the Langmuir binding isotherm yielded $\Delta\varphi_{max}$ of 3.74° and Kd of 10 pM with $R^2 = 0.9987$ (Figure 5(b)), indicating strong and specific binding affinity between DA molecules and the GO-functionalized ZnSe sensing surface. The Kd value reflects the high affinity of the catechol and amine groups of DA for the oxygen-

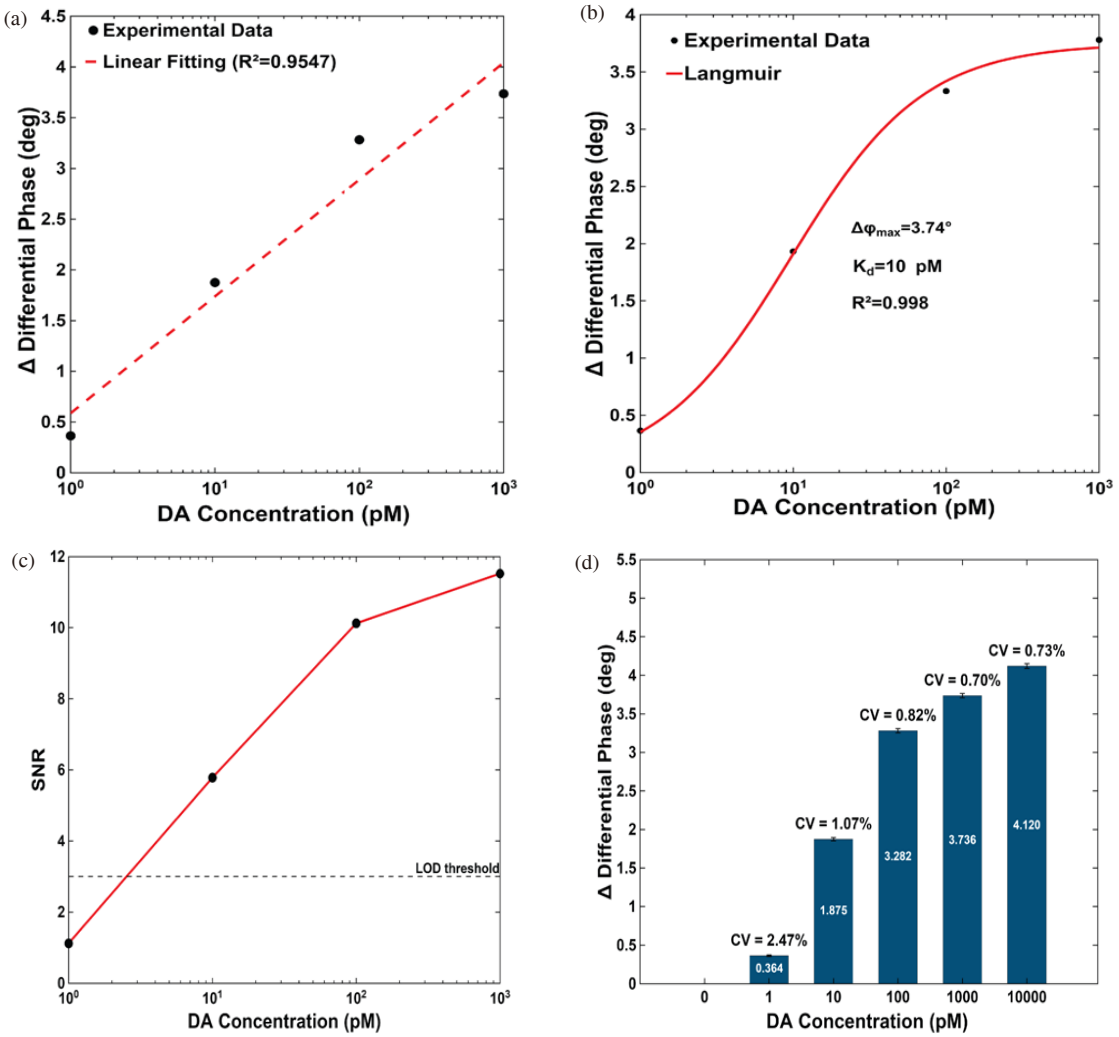

FIGURE 5. Analytical performance of the Ag/ZnSe/APTES/GO biosensor for DA detection: (a) Linear fitting of the differential phase response in the low-concentration regime (1–1000 pM) from independent multi-channel measurements, (b) Langmuir binding isotherm (1 pM–1 nM) from single-channel sequential injection, describing the surface-analyte interaction, with a calculated Kd of 1 pM and a maximum phase shift of 3.74°, (c) SNR as a function of DA concentration, with the dashed line representing the LOD threshold, and (d) intra-chip reproducibility analysis across various concentrations, demonstrating high measurement consistency with low CV values ranging from 0.70% to 2.47%.

rich basal plane and edges of GO, consistent with the preferential and quantitative binding of DA to GO surfaces previously demonstrated by our group [51].

The LOD was determined using the 3σ/slope criterion with intercept correction, where $\sigma = 0.3242°$ represents the standard deviation of the residuals from the semi-log linear fit, yielding a calculated LOD of 2.17 pM. This value corresponds to the SNR = 3 threshold on the fitted calibration curve (Figure 5(c), dashed line). Because 2.17 pM was not experimentally tested, the lowest measured concentration satisfying SNR $\geq$ 3 is 10 pM (SNR = 5.78), which is reported as the experimentally validated detection limit. At 1 pM, the SNR was 1.12, confirming that this concentration lies below the reliable detection threshold and near the practical noise floor of the system. The SNR increased consistently with concentration from 1.12 at 1 pM to 5.78 at 10 pM, 10.12 at 100 pM, and 11.52 at 1 nM. The practical limit of quantification (LOQ) was determined as the lowest tested concentration, achieving SNR $\geq$ 10 and yielding 100 pM (SNR = 10.12). The dominant noise sources include laser intensity fluctuations, detector electronic noise, mechanical vibrations, and thermal drift of the buffer RI, which were mitigated by a 30-minute laser warm-up stabilization period, vibration-isolated optical mounting, and full thermal equilibration at 22°C before each measurement. The intra-chip reproducibility was assessed by performing repeated measurements at each concentration across multiple channels on the same chip. As presented in Figure 5(d), CV values were 2.47% at 1 pM, 1.07% at 10 pM, 0.82% at 100 pM, 0.70% at 1 nM, and 0.73% at 10 nM, all well below 5%, confirming excellent measurement consistency across the sensing channels. To contextualize these results, Table 1 presents a comparison with relevant SPR and other GO-based DA sensors from the literature. In our previous work [51], we developed the first GO-modified SPR sensor for DA detection operating in angular interrogation mode, achieving a sensitivity of 0.2148°/pM, an affinity constant of 2.148 TM^{-1}, and a LOD of 0.1 pM over a linear

TABLE 1. Comparison of the lowest detection limits of DA sensors based on GO without and with other materials.

Material	Detection method	LOD	Linear range	Reference
rGO/MWCNTs/AuNPs/GCE	EC	67 nM	0.20–70 μM	[45]
GO	EC	0.27 μM	1–15 μM	[46]
ERGO	EC	0.1 μM	0.1–10 μM	[47]
ERGO-P/GCE	EC	35 nM	1–500 μM	[48]
PEDOT/rGO/aptamer	EC	78 fM	1 pM–160 nM	[49]
Au@PPy/RGOS	EC	18.29 pM	0.1–5000 nM	[50]
GO/Au	SPR (Angle mode)	0.1 pM	0.1 pM–1 nM	[51]
MWCNT/GONR/GCE[1]	EC	0.08 μM	0.5–50 μM	[60]
AuNPs-rGOS-ITO[2]	EC	60 nM	0.02–40 μM	[61]
AuNPs/ERGO/GCE[3]	EC	0.04 μM	0.1–10 μM	[62]
{AuNPs/RGO}20/GCE	EC	0.02 μM	1–60 μM	[63]
RGO-AuNPs-CSHMs[4]	EC	0.3 μM	1–100 μM	[64]
Pd-RGO/GCE	EC	100 nM	2–10 μM	[65]
Cu-zeolite A/RGO/GCE	EC	41 nM	0.1–19 μM	[66]
Pd Pt/PDDA-RGO[5]	EC	0.04 μM	4–400 μM	[67]
RGO–Pd/GCE	EC	0.233 μM	1–150 μM	[68]
rGO–P*p*PD/GCE[6]	EC	0.36 μM	5–25 μM, 50–200 μM	[69]
Au NPs@ polystyrene /RGO/GCE	EC	5 nM	0.05–20 μM	[70]
Ag NPs/rGO	EC	5.4 μM	10–800 μM	[71]
MWCNT/GO/GCE	EC	22 nM	0.2–400 μM	[72]
Au @Pd–RGO/GCE	EC	2 nM	0.01–100 μM	[73]
Pt/RGO/GCE	EC	0.25 μM	10–170 μM	[74]
ERGO-ferulic aci/GCE	EC	0.19 μM	0.6–1000 μM	[75]
3D–RGO/GCE	EC	0.17 μM	5 μM–1 mM	[76]
ERGO	EC	20 nM	25 nM–5 μM	[77]
(f-RGO)/GCE[7]	EC	3 μM	5–70, 100–600 μM	[78]
Ag NPs/SiO_2/GO/GCE	EC	0.26 μM	2–80 μM	[79]
Au/RGO/GCE	EC	1.4 μM	6.8–41 μM	[80]
CTAB–GO/MWCNT/GCE[8]	EC	1.5 μM	5–500 μM	[81]
ERGO	EC	0.5 μM	0.5–60 μM	[82]
ErGO/CFE	EC	0.77 μM	1.5–224.82 μM	[83]
rGO/TiO_2 {001}/GCE	EC	6 μM	2–60 μM	[84]
Fe_3O_4/rGO/GCE	EC	0.12 μM	0.5 –100 μM	[85]
rGO–CDs/GCE	EC	1.5 nM	10 nM–450 μM	[86]
rGO/Fe_3O_4/GCE	EC	7 nM	0.01–100.55 μM	[87]
poly(L-lysine)/GO/GCE	EC	21 nM	0.5–35 μM	[88]
3D Pgo/Au NP/Porous G /ITO	EC	1.28 μM	0.1–30 μM	[89]
rGO-Co_3O_4/GCE	EC	0.277 μM	1–30 μM	[90]
MnO_2 NWs/ERGO/GCE	EC	1 nM	0.10–1.0, 1.0–80 μM	[91]
PPy/ERGO	EC	23 nM	0.1–150 μM	[92]
RGO-HDPPy/GCE[9]	EC	0.3 nM	1–8000 nM	[93]
GO-PEDOT/GCE[10]	EC	83 nM	1–40 μM	[94]
PEDOT/RGO/GCE	EC	39 nM	0.1–175 μM	[95]
GO/AuNPs/pDAN-EDTA[11]	EC	5 nM	10 nM–1 μM	[96]
PILs/PPy/GO[12]	EC	73.3 nM	4–18 μM	[97]
ET-SDBS-NPPy/ERGO[13]	EC	20 nM	0.1–100 μM	[98]
PEDOT/GO/CFE[14]	EC	0.22 μM	0.5–10 μM	[99]
GO	Fluorescence	94 nM	0.25–20 μM	[100]
Au NP-RGO-$K_2S_2O_8$	ECL[15]	6.2 nM	0.02–40 μM	[101]

rGO/Ag Nanotriangle	Fluorescence	25 μM	50–500 μM	[102]
CuS-rGO	Spectrophotometry	0.48 μM	2–100 μM	[103]
Ag@GO	UV-vis absorption spectrophotometer	30 nM	100 nM–2 μM	[104]
Glass/Ti/Ag/Al_2O_3/ZnSe/APTES/GO	SPR (Phase mode)	10 pM	1–1000 pM	This work

[1]MWCNT: multi-walled carbon nanotubes; GONR: GO nanoribbon.
[2]rGOS: reduced graphene oxide sheets.
[3]ERGO: electrochemically reduced graphene oxide.
[4]CSHMs: chitosan/silica sol–gel hybrid membranes.
[5]PDDA: poly (diallyldimethylammonium chloride).
[6]PpPD: poly (p-phenylenediamine).
[7]f-RGO: flower-like graphene-nanosheet clusters.
[8]CTAB: hexadecyl trimethyl ammonium bromide.
[9]HDPPy: highly dispersed PPy nanospheres.
[10]PEDOT: poly (3,4-ethylenedioxythiophene).
[11]pDAN-EDTA: ethylenediamine triacetic acid immobilized-poly (1,5-diaminonaphthalne).
[12]PILs: poly (ionic liquids).
[13]ET-SDBS-NPPy: electrochemically treated sodium dodecyl benzene sulfonate doped nano PPy.
[14]CFE: carbon fiber electrode.
[15]ECL: electrochemiluminescence.

range of 100 fM to 1 nM. While the reported LOD (0.1 pM) is numerically lower than the 2.17 pM obtained in the present work, it is important to recognize that the 0.1 pM value from the angular mode was similarly derived from 3σ/slope curve fitting rather than from a directly measurable SNR $\geq$ 3 signal. In fact, when the same SNR $\geq$ 3 criterion is applied retrospectively to the angular-mode data, the practically reliable detection limit would be substantially higher than 0.1 pM, because the progressive broadening of the SPR dip (from 3.04° for the bare film to 3.40° at 1 nM DA) resulted in extremely low SNR values throughout the entire sub-nanomolar concentration range. Thus, the apparent superiority of the angular-mode LOD is largely an artifact of the fitting method rather than a reflection of true measurement reliability. The phase-interrogation approach employed in the present work directly addresses this limitation: by extracting the differential phase between P- and S-polarized components rather than tracking the angular position of the reflectance minimum, the measurement is far less susceptible to noise and dip-broadening effects, yielding consistently high SNR and low CV across the tested concentration range. A fairer comparison, therefore, is not between the two numerically reported LODs, but between the practically reliable detection limits defined by the same SNR criterion — under which the present phase-interrogation sensor offers a clear and meaningful improvement over the earlier angular-mode platform. The Ag/Al_2O_3/ZnSe waveguide-coupled structure further contributes to this improvement by confining the evanescent field more effectively at the sensing surface, enhancing the phase sensitivity relative to conventional flat metal film configurations as shown in Figure 3(f). Beyond SPR-based approaches, the broader GO-based DA sensing literature has predominantly relied on electrochemical transduction. Representative works include bare GO electrodes achieving LODs in the range of 0.1 to 0.27 μM [46, 47], composite platforms such as ERGO-porphyrin reaching an LOD of 35 nM [48], and aptamer-functionalized conducting polymer/GO composites achieving LODs as low as 78 fM [49]. While some of these electrochemical approaches achieve lower absolute detection limits through signal amplification strategies, they generally require more complex surface chemistry, are susceptible to electrode fouling, and cannot provide the real-time kinetic information that SPR-based phase interrogation inherently delivers. The present sensor combines the surface affinity advantages of GO with the measurement reliability of phase-interrogation SPR and the practical throughput of ten-channel microfluidic integration, representing a meaningful advance over both our earlier angular SPR platform and existing electrochemical GO-based DA sensors. Importantly, this improvement is not merely a matter of achieving a lower numerically fitted LOD, but of delivering reliable, high-SNR measurements at trace concentrations (a capability that the angular-mode platform could not provide due to resonance broadening induced by the GO functional layer). This study was conducted under controlled PBS buffer conditions. Future work will focus on testing in complex biological matrices, assessing selectivity against potential interferences, and integrating aptamers or molecularly imprinted polymers to enhance specificity and achieve femtomolar-level detection.

GO served as an effective capture material for DA due to its surface chemistry. The basal plane and edges of GO carry carboxyl, hydroxyl, and epoxy groups that engage DA through several mechanisms at once: π-π stacking with the aromatic ring, hydrogen bonding with the catechol hydroxyls, and electrostatic attraction between DA's protonated amine (pKa $\sim$ 8.9) and the negatively charged carboxylates at physiological pH 7.4. This combination of interactions working together gives GO its strong natural affinity for DA, as reflected in the Langmuir dissociation constant of 10 pM obtained here, which is reasonably close to the binding affinity of 2.148 TM^{-1} we reported previously [51], with the small difference likely coming from how the GO layer was deposited in each case: spin coating in [51] versus injection through microfluidic channels in this work, two approaches that can produce different layer thicknesses, surface coverage, and ultimately the number of binding

sites available to DA. GO's large surface area and hydrophilic character further support efficient DA transport to the sensing surface under flow [43], and EC studies confirm that its oxygen functional groups and extended conjugated structure actively accelerate the interaction [48]. In the SPR context, GO also plays an optical role: its relatively high RI amplifies the dielectric perturbation at the ZnSe surface upon DA adsorption, increasing the phase shift per bound molecule [59]. The same cooperative binding that favors DA also works against common interferences, such as AA and UA, which lack the complementary structural features needed to engage GO in the same way [51]. The APTES mediated immobilization strategy is equally critical: silanization generates a stable amine terminated monolayer that electrostatically anchors negatively charged GO [43], yielding robust surface coverage resistant to aqueous flow while maximizing active binding site availability for DA capture.

The present work makes four distinct contributions that have not been previously demonstrated. First, we identify a fundamental but previously unreported reliability failure in angular-mode GO/SPR DA sensors: the previously reported LOD of 0.1 pM was a purely statistical artifact of curve fitting applied to data containing no reliably detectable signal, as the maximum SNR across the entire tested concentration range never reached the SNR $= 3$ detection threshold. Second, we introduce for the first time a ZnSe waveguide-coupled SPR platform operating under phase interrogation for DA detection. ZnSe achieves superior resonance confinement owing to its high refractive index, yielding 2.6-fold narrower FWHM, 5-fold higher FOM (1527 vs. 300 RIU^{-1}), and 2-fold higher angular sensitivity (120.1 vs. 60 deg/RIU) relative to previously reported SiO_2-based waveguide SPR. Critically, while the SiO_2-based platform demonstrated detection of a large protein (α-synuclein, ~ 14 kDa), the present work addresses DA, a small molecule of only 0.189 kDa representing $\sim$ 76-fold lower molecular weight and significantly lower polarizability, using a fundamentally different surface chemistry (APTES/GO for direct molecular capture), with validated binding kinetics (Langmuir Kd $= 10$ pM) and quantified intra-chip reproducibility (CV 0.70–2.47%), delivering the first SNR-validated picomolar small-molecule detection on a GO-functionalized waveguide SPR platform. Third, we provide the first direct performance comparison between angular and phase interrogation modes on GO/SPR DA sensors using a common SNR criterion, establishing that the practical LOD of angular mode is undefined while phase interrogation delivers a validated LOD of 10 pM with quantified intra-chip reproducibility. Fourth, compared to solution-phase GO-based optical DA sensors exploiting Ag@GO nanocomposites in UV-Vis spectrophotometry [103], which report LODs in the 30 to 49 nM range with no kinetic information, the present surface-confined phase interrogation platform offers orders-of-magnitude improvement in detection capability together with real-time binding information. Collectively, this work resolves the SNR failure mode undermining reported LODs in angular GO/SPR DA sensors, establishes ZnSe as a superior high-index waveguide material for phase-mode SPR, and delivers the first fully noise-validated picomolar DA sensor on a GO-functionalized SPR platform.

While high-performance liquid chromatography with EC detection (HPLC-ECD) serves as the clinical gold standard for DA quantification, it requires high-cost instrumentation, extensive sample preparation, and trained personnel, rendering it unsuitable for real-time or point-of-care applications [105]. Similarly, ELISA-based approaches offer standardized clinical diagnostic pathways but rely on multi-hour, batch-mode processing and expensive, single-use enzymatic reagents that are incompatible with the rapid monitoring needs of therapeutic drug monitoring (TDM) [106]. Among EC platforms, advanced nanocomposite-based sensors have achieved competitive limits of detection; for example, 70 pM using a flexible LIG-$Nb_4C_3T_x$IMXene-PPy-FeNPs electrode [107], and sub-femtomolar levels using Nb_2CT_x@MoS_2 heterostructures [108]. Yet these platforms frequently face challenges regarding surface fouling and interference from common physiological co-analytes, such as AA and UA. Furthermore, existing SPR-based biosensors utilizing enzymatic laccase functionalization have reported sensitivities in the 0.1 ng/mL range [109], which is significantly less sensitive than the picomolar-level detection achieved by our platform. In contrast, our phase-interrogated SPR sensor provides a practical LOD of 10 pM and a linear dynamic range (1 pM–1 nM) that directly encompasses the physiologically relevant concentrations of DA in blood ($<$ 130 pM). By operating as a direct sensing architecture that eliminates the need for enzymatic reagents, EC oxidation, or complex sample derivatization, our platform significantly reduces operational complexity and sample volume, offering a robust, scalable alternative for future clinical neurochemical monitoring.

In this work, all measurements were conducted at controlled room temperature (22°C), with sufficient thermal equilibration time prior to data acquisition to minimize baseline drift. Given the high phase sensitivity of 4.53×10^4 deg RIU^{-1}, temperature stability is important, as the RI of aqueous media varies at approximately -1.06×10^{-4} RIU/°C at ~ 25°C and 635 nm [110], meaning even minor temperature fluctuations can produce measurable phase shifts that could be mistaken for analyte binding at trace concentrations. The low intra-chip CVs of 0.70–2.47% confirm that thermal stability was adequately maintained under the present conditions. For pharmaceutical applications, the sensor would typically operate at a fixed, regulated temperature, either ambient (22°C) for standard analytical workflows or physiological temperature (37°C) for biomimetic binding studies. Active Peltier stabilization would ensure this set point is maintained regardless of environmental conditions, and the measurement protocol would include temperature logging as part of the quality system.

4. CONCLUSION

We have presented a phase-interrogated SPR biosensor built on a GO-functionalized Ag/ZnSe multilayer that achieves reliable, direct DA detection at picomolar concentrations. The ZnSe layer supported a waveguide-coupled plasmon mode that narrowed the SPR dips and produced the abrupt phase jump. The fabricated sensor yielded an FWHM of 0.077°, a Q-factor of 799, and an FOM of 1527 RIU^{-1}. The small deviation

from the simulated FWHM of 0.034° is consistent with practical fabrication imperfections and beam angular divergence rather than any fundamental design limitation. Glucose calibration established a phase sensitivity of 4.53×10^4 deg RIU^{-1} alongside an angular sensitivity of 120.1°/RIU. For DA, the APTES/GO-functionalized surface showed a semi-log linear sensitivity of 1.15°/decade ($R^2 = 0.9547$) over 1 pM to 1 nM, a Langmuir dissociation constant of 10 pM ($R^2 = 0.998$), a practical LOD of 10 pM, and intra-chip CVs between 0.70% and 2.47%. These figures compare favorably with our earlier GO-based angular SPR platform, where progressive resonance broadening upon surface functionalization degraded the FOM and compromised measurement reliability at trace concentrations. The phase-interrogation approach resolves this by decoupling sensitivity from dip width, maintaining high SNR across the full DA concentration range without requiring complex instrumentation. Beyond its demonstrated performance in buffer conditions, this platform holds significant potential for pharmaceutical applications. The ability to detect DA reliably at picomolar levels is directly relevant to drug development programs targeting dopaminergic dysfunction, where the precise measurement of drug candidates' effects on DA levels in preclinical models and clinical trials is essential for pharmacokinetic/pharmacodynamic (PK/PD) profiling, dose optimization, and safety assessment. Moreover, the microfluidic integration and rapid readout make this sensor compatible with therapeutic drug monitoring (TDM) and near-patient testing scenarios, aligning with the growing emphasis on personalized medicine in the pharmaceutical industry. The current limitation is that all measurements were carried out in PBS buffer under controlled conditions. Testing in real biological matrices such as serum and cerebrospinal fluid, incorporating selective recognition elements such as aptamers or molecularly imprinted polymers to strengthen discrimination against structurally similar interferents, and verifying reproducibility across independently fabricated chips remain the priorities for the next stage of development. With its simple two-step surface chemistry, ten-channel microfluidic throughput, and strong phase sensitivity, this platform offers a practical and scalable route toward point-of-care DA monitoring in neurological disease management and holds promise as a versatile tool for pharmaceutical R&D and clinical translation.

ACKNOWLEDGEMENT

This work was jointly supported by the Science and Technology Plan Key Project of Taizhou City (24gyz01), Science and Technology Plan Project of Luqiao (Taizhou) District (2024G2009), and Zhejiang Provincial Health Commission (CXTD202502029), "Pioneer" and "Leading Goose" R&D Program of Zhejiang Province (2024C03045). The authors are also grateful to Dr. Julian Evans of Zhejiang University for helpful discussion.

REFERENCES

[1] Yusoff, N., A. Pandikumar, R. Ramaraj, H. Lim, and N. Huang, "Gold nanoparticle based optical and electrochemical sensing of dopamine," *Microchimica Acta*, Vol. 182, 2091–2114, 2015.

[2] Suhito, I. R., N. Angeline, and T.-H. Kim, "Nanomaterial-modified hybrid platforms for precise electrochemical detection of dopamine," *Biochip Journal*, Vol. 13, No. 1, 20–29, 2019.

[3] Kujawska, M., S. K. Bhardwaj, Y. K. Mishra, and A. Kaushik, "Using graphene-based biosensors to detect dopamine for efficient Parkinson's disease diagnostics," *Biosensors*, Vol. 11, No. 11, 433, 2021.

[4] Sun, X., L. Zhang, X. Zhang, X. Liu, J. Jian, D. Kong, D. Zeng, H. Yuan, and S. Feng, "Electrochemical dopamine sensor based on superionic conducting potassium ferrite," *Biosensors and Bioelectronics*, Vol. 153, 112045, 2020.

[5] Cai, L., B. Hou, Y. Shang, L. Xu, B. Zhou, X. Jiang, and X. Jiang, "Synthesis of Fe_3O_4/graphene oxide/pristine graphene ternary composite and fabrication electrochemical sensor to detect dopamine and hydrogen peroxide," *Chemical Physics Letters*, Vol. 736, 136797, 2019.

[6] Sarno, M., S. Galvagno, C. Scudieri, P. Iovane, S. Portofino, C. Borriello, and C. Cirillo, "Dopamine sensor in real sample based on thermal plasma silicon carbide nanopowders," *Journal of Physics and Chemistry of Solids*, Vol. 131, 213–222, 2019.

[7] Kokulnathan, T., T.-J. Wang, E. A. Kumar, N. Duraisamy, and A.-T. Lee, "An electrochemical platform based on yttrium oxide/boron nitride nanocomposite for the detection of dopamine," *Sensors and Actuators B: Chemical*, Vol. 349, 130787, 2021.

[8] Bui, M.-P. N., C. A. Li, and G. H. Seong, "Electrochemical detection of dopamine with poly-glutamic acid patterned carbon nanotube electrodes," *Biochip Journal*, Vol. 6, No. 2, 149–156, 2012.

[9] Hows, M. E. P., L. Lacroix, C. Heidbreder, A. J. Organ, and A. J. Shah, "High-performance liquid chromatography/tandem mass spectrometric assay for the simultaneous measurement of dopamine, norepinephrine, 5-hydroxytryptamine and cocaine in biological samples," *Journal of Neuroscience Methods*, Vol. 138, No. 1-2, 123–132, 2004.

[10] Carrera, V., E. Sabater, E. Vilanova, and M. A. Sogorb, "A simple and rapid HPLC-MS method for the simultaneous determination of epinephrine, norepinephrine, dopamine and 5-hydroxytryptamine: Application to the secretion of bovine chromaffin cell cultures," *Journal of Chromatography B*, Vol. 847, No. 2, 88–94, 2007.

[11] Wang, H. Y., Q. S. Hui, L. X. Xu, J. G. Jiang, and Y. Sun, "Fluorimetric determination of dopamine in pharmaceutical products and urine using ethylene diamine as the fluorigenic reagent," *Analytica Chimica Acta*, Vol. 497, No. 1–2, 93–99, 2003.

[12] Kruss, S., M. P. Landry, E. V. Ende, B. M. A. Lima, N. F. Reuel, J. Zhang, J. Nelson, B. Mu, A. Hilmer, and M. Strano, "Neurotransmitter detection using corona phase molecular recognition on fluorescent single-walled carbon nanotube sensors," *Journal of The American Chemical Society*, Vol. 136, No. 2, 713–724, 2014.

[13] Zhu, Q., Y. Chen, W. Wang, H. Zhang, C. Ren, H. Chen, and X. Chen, "A sensitive biosensor for dopamine determination based on the unique catalytic chemiluminescence of metal-organic framework hkust-1," *Sensors and Actuators B: Chemical*, Vol. 210, 500–507, 2015.

[14] Syslová, K., L. Rambousek, M. Kuzma, V. Najmanová, V. Bubeníková-Valešová, R. Šlamberová, and P. Kačer, "Monitoring of dopamine and its metabolites in brain microdialysates: Method combining freeze-drying with liquid chromatography-tandem mass spectrometry," *Journal of Chromatography A*,

Vol. 1218, No. 21, 3382–3391, 2011.

[15] Zhao, Y., S. Zhao, J. Huang, and F. Ye, "Quantum dot-enhanced chemiluminescence detection for simultaneous determination of dopamine and epinephrine by capillary electrophoresis," *Talanta*, Vol. 85, No. 5, 2650–2654, 2011.

[16] Guan, Q., H. Guo, R. Xue, M. Wang, X. Zhao, T. Fan, W. Yang, M. Xu, and W. Yang, "Electrochemical sensor based on covalent organic frameworks-MWCNT-NH_2/AuNPs for simultaneous detection of dopamine and uric acid," *Journal of Electroanalytical Chemistry*, Vol. 880, 114932, 2021.

[17] Homola, J., "Surface plasmon resonance sensors for detection of chemical and biological species," *Chemical Reviews*, Vol. 108, No. 2, 462–493, 2008.

[18] Caucheteur, C., T. Guo, and J. Albert, "Review of plasmonic fiber optic biochemical sensors: Improving the limit of detection," *Analytical and Bioanalytical Chemistry*, Vol. 407, No. 14, 3883–3897, 2015.

[19] Daniyal, W. M. E. M. M., Y. W. Fen, F. B. Kamal Eddin, J. Abdullah, and M. A. Mahdi, "Surface plasmon resonance assisted optical characterization of nickel ion solution and nanocrystalline cellulose-graphene oxide thin film for sensitivity enhancement analysis," *Physica B: Condensed Matter*, Vol. 646, 414292, 2022.

[20] Kamal Eddin, F. B., Y. W. Fen, J. Y. C. Liew, and W. M. E. M. M. Daniyal, "Plasmonic refractive index sensor enhanced with chitosan/au bilayer thin film for dopamine detection," *Biosensors*, Vol. 12, No. 12, 1124, 2022.

[21] Ishimaru, A., S. Jaruwatanadilok, and Y. Kuga, "Generalized surface plasmon resonance sensors using metamaterials and negative index materials," *Progress In Electromagnetics Research*, Vol. 51, 139–152, 2005.

[22] Pitarke, J. M., V. M. Silkin, E. V. Chulkov, and P. M. Echenique, "Theory of surface plasmons and surface-plasmon polaritons," *Reports on Progress in Physics*, Vol. 70, No. 1, 1–87, 2007.

[23] Chau, Y.-F. C., "Advances in Fano resonance-based metal-insulator-metal plasmonic sensors: Mechanisms, applications, and future perspectives," *Optics & Laser Technology*, Vol. 194, 114487, 2026.

[24] Chao, C. T. C. and Y.-F. C. Chau, "Engineering plasmonic photonic crystal fiber sensors: Design, fabrication strategies, and performance roadmap," *Materials Science and Engineering: B*, Vol. 324, 119046, 2026.

[25] Chau, Y.-F. C., S.-H. Chen, A. H. Mahadi, R. Thotagamuge, C. M. Lim, and M. R. R. Kooh, "Plasmonic-heterojunction nanostructures: Mechanistic design for photocatalysis, energy conversion, and advanced biosensing," *Sustainable Materials and Technologies*, Vol. 47, e01833, 2025.

[26] Chau, Y.-F. C., "Converging nanophotonics and environmental science: Plasmonic biosensors for smart, distributed monitoring," *Journal of Environmental Chemical Engineering*, Vol. 14, 123224, 2026.

[27] Chau, Y.-F. C., "Plasmonics in environmental sensing, pollution monitoring, and sustainable applications," *Materials Today Physics*, Vol. 60, 101984, 2025.

[28] Chau, Y.-F. C., "Plasmonics-enabled advanced technologies for water purification, desalination, and environmental monitoring," *Process Safety and Environmental Protection*, Vol. 207, 108420, 2026.

[29] Xu, Z., W. Zhang, C. Quesada, X. Wang, and M. Fabiilli, "Longitudinal monitoring of angiogenesis in a murine window chamber model in vivo," *Tissue Engineering Part C: Methods*, Vol. 30, No. 3, 93–101, 2024.

[30] Xu, Z., Y. Jiang, J. Ji, E. Forsberg, Y. Li, and S. He, "Classification, identification, and growth stage estimation of microalgae based on transmission hyperspectral microscopic imaging and machine learning," *Optics Express*, Vol. 28, No. 21, 30 686–30 700, 2020.

[31] Jiao, C., Z. Xu, Q. Bian, E. Forsberg, Q. Tan, X. Peng, and S. He, "Machine learning classification of origins and varieties of Tetrastigma hemsleyanum using a dual-mode microscopic hyperspectral imager," *Spectrochimica Acta Part A: Molecular and Biomolecular Spectroscopy*, Vol. 261, 120054, 2021.

[32] Xu, Z., G. Escalona, I. Schrack, W. Zhang, T. Zhai, L. D. Shea, and X. Wang, "Detecting metastatic potential of cancer through longitudinal vasculature imaging of biomaterial scaffold using non-invasive in vivo photoacoustic microscopy and optical coherence tomography," *Theranostics*, Vol. 15, No. 2, 509–520, 2025.

[33] Xu, Z., Y. Jiang, and S. He, "Multi-mode microscopic hyperspectral imager for the sensing of biological samples," *Applied Sciences*, Vol. 10, No. 14, 4876, 2020.

[34] Xu, Z., C. S. Locke, R. Morris, D. Jamison, K. M. Kozloff, and X. Wang, "Development of a semi-anthropomorphic photoacoustic calcaneus phantom based on nano computed tomography and stereolithography 3d printing," *Journal of Orthopaedic Research*, Vol. 42, No. 3, 647–660, 2024.

[35] Chao, C.-T. C., S.-H. Chen, H. J. Huang, M. R. R. Kooh, C. M. Lim, R. Thotagamuge, A. H. Mahadi, and Y.-F. C. Chau, "Improving temperature-sensing performance of photonic crystal fiber via external metal-coated trapezoidal-shaped surface," *Crystals*, Vol. 13, No. 5, 813, 2023.

[36] Sabaruddin, N. R., Y. M. Tan, C.-T. C. Chao, M. R. R. Kooh, and Y.-F. C. Chau, "High sensitivity of metasurface-based five-band terahertz absorber," *Plasmonics*, Vol. 19, No. 1, 481–493, 2024.

[37] Sabaruddin, N. R., Y. M. Tan, S.-H. Chen, C.-T. C. Chao, C. M. Lim, R. Thotagamuge, M. R. R. Kooh, and Y.-F. C. Chau, "Designing a broadband terahertz metamaterial absorber through bi-layer hybridization of metal and graphene," *Plasmonics*, Vol. 19, No. 6, 3259–3272, 2024.

[38] Chau, Y.-F. C., S.-H. Chen, H. J. Huang, R. Thotagamuge, and M. R. R. Kooh, "Multi-mode and bidirectional plasmonic metamaterial absorber based on bilayer graphene and bowtie-shaped windows," *Optical and Quantum Electronics*, Vol. 57, No. 12, 630, 2025.

[39] Wang, T., Y. Kang, L. Jiang, Z. Zheng, and S. Liang, "Enhanced sensitivity of SPR sensor using Au@Bi_2Se_3 core-shell nanoparticles and lead ion detection]," *IEEE Sensors Journal*, Vol. 25, 37 909–37 915, 2025.

[40] Yang, K., Y. Chen, S. Yan, and W. Yang, "Nanostructured surface plasmon resonance sensors: Toward narrow linewidths," *Heliyon*, Vol. 9, No. 6, e16598, 2023.

[41] Chen, X. and W. Kong, "Theoretical analysis of relationship between quasi-BIC and intrinsic parameters in surface plasmon resonance sensors," *Chinese Optics Letters*, Vol. 23, No. 11, 111201, 2025.

[42] Liu, Z., T. Guo, Q. Tan, H. Fan, and S. He, "Guided mode induced surface phase mutation for enhanced SPR biosensor with dual-parameters interrogation," *Advanced Materials Interfaces*, Vol. 10, No. 34, 2300354, 2023.

[43] Zhang, P., M. He, and Y. Zeng, "Ultrasensitive microfluidic analysis of circulating exosomes using a nanostructured graphene oxide/polydopamine coating," *Lab on A Chip*, Vol. 16, No. 16, 3033–3042, 2016.

[44] Teymourian, H., A. Salimi, and S. Khezrian, "Fe_3O_4 magnetic nanoparticles/reduced graphene oxide nanosheets as a novel electrochemical and bioeletrochemical sensing platform," *Biosensors and Bioelectronics*, Vol. 49, 1–8, 2013.

[45] Yuan, D., S. Chen, R. Yuan, J. Zhang, and X. Liu, "An ECL sensor for dopamine using reduced graphene oxide/multiwall carbon nanotubes/gold nanoparticles," *Sensors and Actuators B: Chemical*, Vol. 191, 415–420, 2014.

[46] Gao, F., X. Cai, X. Wang, C. Gao, S. Liu, F. Gao, and Q. Wang, "Highly sensitive and selective detection of dopamine in the presence of ascorbic acid at graphene oxide modified electrode," *Sensors and Actuators B: Chemical*, Vol. 186, 380–387, 2013.

[47] Yu, X., K. Sheng, and G. Shi, "A three-dimensional interpenetrating electrode of reduced graphene oxide for selective detection of dopamine," *Analyst*, Vol. 139, No. 18, 4525–4531, 2014.

[48] Han, H. S., H. K. Lee, J.-M. You, H. Jeong, and S. Jeon, "Electrochemical biosensor for simultaneous determination of dopamine and serotonin based on electrochemically reduced GO-porphyrin," *Sensors and Actuators B: Chemical*, Vol. 190, 886–895, 2014.

[49] Wang, W., W. Wang, J. J. Davis, and X. Luo, "Ultrasensitive and selective voltammetric aptasensor for dopamine based on a conducting polymer nanocomposite doped with graphene oxide," *Microchimica Acta*, Vol. 182, No. 5, 1123–1129, 2015.

[50] Qian, T., C. Yu, X. Zhou, S. Wu, and J. Shen, "Au nanoparticles decorated polypyrrole/reduced graphene oxide hybrid sheets for ultrasensitive dopamine detection," *Sensors and Actuators B: Chemical*, Vol. 193, 759–763, 2014.

[51] Kamal Eddin, F. B., Y. W. Fen, J. Y. C. Liew, N. I. M. Fauzi, W. M. E. M. M. Daniyal, and H. Abdullah, "Development of plasmonic-based sensor for highly sensitive and selective detection of dopamine," *Optics & Laser Technology*, Vol. 161, 109221, 2023.

[52] Yeh, P., *Optical Waves in Layered Media*, Wiley, 1988.

[53] Ouyang, Q., S. Zeng, L. Jiang, L. Hong, G. Xu, X.-Q. Dinh, J. Qian, S. He, J. Qu, P. Coquet, *et al.*, "Sensitivity enhancement of transition metal dichalcogenides/silicon nanostructure-based surface plasmon resonance biosensor," *Scientific Reports*, Vol. 6, No. 1, 28190, 2016.

[54] Araguillin-López, R. D., A. D. Méndez-Cevallos, and C. Costa-Vera, "Detailed modeling of surface-plasmon resonance spectrometer response for accurate correction," *Sensors*, Vol. 25, No. 3, 894, 2025.

[55] Raether, H., *Surface Plasmons on Smooth and Rough Surfaces and on Gratings*, Springer, 1988.

[56] Kretschmann, E. and H. Raether, "Radiative decay of non radiative surface plasmons excited by light," *Z. Naturforsch. A*, Vol. 23, No. 12, 2135–2136, 1968.

[57] Otto, A., "Excitation of nonradiative surface plasma waves in silver by the method of frustrated total reflection," *Z. Phys.*, Vol. 216, No. 4, 398–410, 1968.

[58] Lide, D. R., *CRC Handbook of Chemistry and Physics*, Internet Version 2005, CRC Press, 2005.

[59] Kamal Eddin, F. B., Y. W. Fen, J. Y. C. Liew, H. N. Lim, W. M. E. M. M. Daniyal, and N. A. S. Omar, "Simultaneous measurement of the refractive index and thickness of graphene oxide/gold multilayered structure for potential in dopamine sensing using surface plasmon resonance spectroscopy," *Optik*, Vol. 278, 170703, 2023.

[60] Sun, C.-L., C.-T. Chang, H.-H. Lee, J. Zhou, J. Wang, T.-K. Sham, and W.-F. Pong, "Microwave-assisted synthesis of a core-shell MWCNT/GONR heterostructure for the electrochemical detection of ascorbic acid, dopamine, and uric acid," *ACS Nano*, Vol. 5, No. 10, 7788–7795, 2011.

[61] Yang, J., J. R. Strickler, and S. Gunasekaran, "Indium tin oxide-coated glass modified with reduced graphene oxide sheets and gold nanoparticles as disposable working electrodes for dopamine sensing in meat samples," *Nanoscale*, Vol. 4, No. 15, 4594–4602, 2012.

[62] Li, S.-J., D.-H. Deng, Q. Shi, and S.-R. Liu, "Electrochemical synthesis of a graphene sheet and gold nanoparticle-based nanocomposite, and its application to amperometric sensing of dopamine," *Microchimica Acta*, Vol. 177, No. 3, 325–331, 2012.

[63] Liu, S., J. Yan, G. He, D. Zhong, J. Chen, L. Shi, X. Zhou, and H. Jiang, "Layer-by-layer assembled multilayer films of reduced graphene oxide/gold nanoparticles for the electrochemical detection of dopamine," *Journal of Electroanalytical Chemistry*, Vol. 672, 40–44, 2012.

[64] Liu, X., L. Xie, and H. Li, "Electrochemical biosensor based on reduced graphene oxide and Au nanoparticles entrapped in chitosan/silica sol-gel hybrid membranes for determination of dopamine and uric acid," *Journal of Electroanalytical Chemistry*, Vol. 682, 158–163, 2012.

[65] Wu, C.-H., C.-H. Wang, M.-T. Lee, and J.-K. Chang, "Unique Pd/graphene nanocomposites constructed using supercritical fluid for superior electrochemical sensing performance," *Journal of Materials Chemistry*, Vol. 22, No. 40, 21 466–21 471, 2012.

[66] He, P., W. Wang, L. Du, F. Dong, Y. Deng, and T. Zhang, "Zeolite a functionalized with copper nanoparticles and graphene oxide for simultaneous electrochemical determination of dopamine and ascorbic acid," *Analytica Chimica Acta*, Vol. 739, 25–30, 2012.

[67] Yan, J., S. Liu, Z. Zhang, G. He, P. Zhou, H. Liang, L. Tian, X. Zhou, and H. Jiang, "Simultaneous electrochemical detection of ascorbic acid, dopamine and uric acid based on graphene anchored with pd-pt nanoparticles," *Colloids and Surfaces B: Biointerfaces*, Vol. 111, 392–397, 2013.

[68] Palanisamy, S., S. Ku, and S.-M. Chen, "Dopamine sensor based on a glassy carbon electrode modified with a reduced graphene oxide and palladium nanoparticles composite," *Microchimica Acta*, Vol. 180, 1037–1042, 2013.

[69] Liu, S., B. Yu, and T. Zhang, "Preparation of crumpled reduced graphene oxide-poly (p-phenylenediamine) hybrids for the detection of dopamine," *Journal of Materials Chemistry A*, Vol. 1, No. 42, 13 314–13 320, 2013.

[70] Qian, T., C. Yu, S. Wu, and J. Shen, "Gold nanoparticles coated polystyrene/reduced graphite oxide microspheres with improved dispersibility and electrical conductivity for dopamine detection," *Colloids and Surfaces B: Biointerfaces*, Vol. 112, 310–314, 2013.

[71] Kaur, B., T. Pandiyan, B. Satpati, and R. Srivastava, "Simultaneous and sensitive determination of ascorbic acid, dopamine, uric acid, and tryptophan with silver nanoparticles-decorated reduced graphene oxide modified electrode," *Colloids and Surfaces B: Biointerfaces*, Vol. 111, 97–106, 2013.

[72] Cheemalapati, S., S. Palanisamy, V. Mani, and S.-M. Chen, "Simultaneous electrochemical determination of dopamine and paracetamol on multiwalled carbon nanotubes/graphene oxide nanocomposite-modified glassy carbon electrode," *Talanta*, Vol. 117, 297–304, 2013.

[73] Jiang, J. and X. Du, "Sensitive electrochemical sensors for simultaneous determination of ascorbic acid, dopamine, and uric

acid based on Au@Pd-reduced graphene oxide nanocomposites," *Nanoscale*, Vol. 6, No. 19, 11 303–11 309, 2014.

[74] Xu, T.-Q., Q.-L. Zhang, J.-N. Zheng, Z.-Y. Lv, J. Wei, A.-J. Wang, and J.-J. Feng, "Simultaneous determination of dopamine and uric acid in the presence of ascorbic acid using Pt nanoparticles supported on reduced graphene oxide," *Electrochimica Acta*, Vol. 115, 109–115, 2014.

[75] Han, H. S., H. Seol, D. H. Kang, M. S. Ahmed, J.-M. You, and S. Jeon, "Electrochemical oxidation and determination of dopamine in the presence of AA using ferulic acid functionalized electrochemically reduced graphene," *Sensors and Actuators B: Chemical*, Vol. 204, 289–296, 2014.

[76] Yu, B., D. Kuang, S. Liu, C. Liu, and T. Zhang, "Template-assisted self-assembly method to prepare three-dimensional reduced graphene oxide for dopamine sensing," *Sensors and Actuators B: Chemical*, Vol. 205, 120–126, 2014.

[77] Zhang, Z., J. Yan, H. Jin, and J. Yin, "Tuning the reduction extent of electrochemically reduced graphene oxide electrode film to enhance its detection limit for voltammetric analysis," *Electrochimica Acta*, Vol. 139, 232–237, 2014.

[78] Wang, H., F. Ren, R. Yue, C. Wang, C. Zhai, and Y. Du, "Macroporous flower-like graphene-nanosheet clusters used for electrochemical determination of dopamine," *Colloids and Surfaces A: Physicochemical and Engineering Aspects*, Vol. 448, 181–185, 2014.

[79] Cincotto, F. H., T. C. Canevari, A. M. Campos, R. Landers, and S. A. S. Machado, "Simultaneous determination of epinephrine and dopamine by electrochemical reduction on the hybrid material SiO_2/graphene oxide decorated with Ag nanoparticles," *Analyst*, Vol. 139, No. 18, 4634–4640, 2014.

[80] Wang, C., J. Du, H. Wang, C. Zou, F. Jiang, P. Yang, and Y. Du, "A facile electrochemical sensor based on reduced graphene oxide and au nanoplates modified glassy carbon electrode for simultaneous detection of ascorbic acid, dopamine and uric acid," *Sensors and Actuators B: Chemical*, Vol. 204, 302–309, 2014.

[81] Yang, Y. J. and W. Li, "CTAB functionalized graphene oxide/multiwalled carbon nanotube composite modified electrode for the simultaneous determination of ascorbic acid, dopamine, uric acid and nitrite," *Biosensors and Bioelectronics*, Vol. 56, 300–306, 2014.

[82] Yang, L., D. Liu, J. Huang, and T. You, "Simultaneous determination of dopamine, ascorbic acid and uric acid at electrochemically reduced graphene oxide modified electrode," *Sensors and Actuators B: Chemical*, Vol. 193, 166–172, 2014.

[83] Yang, B., H. Wang, J. Du, Y. Fu, P. Yang, and Y. Du, "Direct electrodeposition of reduced graphene oxide on carbon fiber electrode for simultaneous determination of ascorbic acid, dopamine and uric acid," *Colloids and Surfaces A: Physicochemical and Engineering Aspects*, Vol. 456, 146–152, 2014.

[84] How, G. T. S., A. Pandikumar, H. N. Ming, and L. H. Ngee, "Highly exposed 001 facets of titanium dioxide modified with reduced graphene oxide for dopamine sensing," *Scientific Reports*, Vol. 4, No. 1, 5044, 2014.

[85] Peik-See, T., A. Pandikumar, H. Nay-Ming, L. Hong-Ngee, and Y. Sulaiman, "Simultaneous electrochemical detection of dopamine and ascorbic acid using an iron oxide/reduced graphene oxide modified glassy carbon electrode," *Sensors*, Vol. 14, No. 8, 15 227–15 243, 2014.

[86] Hu, S., Q. Huang, Y. Lin, C. Wei, H. Zhang, W. Zhang, Z. Guo, X. Bao, J. Shi, and A. Hao, "Reduced graphene oxide-carbon dots composite as an enhanced material for electrochemical determination of dopamine," *Electrochimica Acta*, Vol. 130, 805–809, 2014.

[87] Salamon, J., Y. Sathishkumar, K. Ramachandran, Y. S. Lee, D. J. Yoo, A. R. Kim, *et al.*, "One-pot synthesis of magnetite nanorods/graphene composites and its catalytic activity toward electrochemical detection of dopamine," *Biosensors and Bioelectronics*, Vol. 64, 269–276, 2015.

[88] Zhang, Y., W. Lei, Y. Xu, X. Xia, and Q. Hao, "Simultaneous detection of dopamine and uric acid using a poly (L-lysine)/graphene oxide modified electrode," *Nanomaterials*, Vol. 6, No. 10, 178, 2016.

[89] Choo, S.-S., E.-S. Kang, I. Song, D. Lee, J.-W. Choi, and T.-H. Kim, "Electrochemical detection of dopamine using 3D porous graphene oxide/gold nanoparticle composites," *Sensors*, Vol. 17, No. 4, 861, 2017.

[90] Numan, A., M. M. Shahid, F. S. Omar, K. Ramesh, and S. Ramesh, "Facile fabrication of cobalt oxide nanograin-decorated reduced graphene oxide composite as ultrasensitive platform for dopamine detection," *Sensors and Actuators B: Chemical*, Vol. 238, 1043–1051, 2017.

[91] He, Q., J. Liu, X. Liu, G. Li, D. Chen, P. Deng, and J. Liang, "A promising sensing platform toward dopamine using MnO_2 nanowires/electro-reduced graphene oxide composites," *Electrochimica Acta*, Vol. 296, 683–692, 2019.

[92] Si, P., H. Chen, P. Kannan, and D.-H. Kim, "Selective and sensitive determination of dopamine by composites of polypyrrole and graphene modified electrodes," *Analyst*, Vol. 136, No. 24, 5134–5138, 2011.

[93] Qian, T., C. Yu, S. Wu, and J. Shen, "In situ polymerization of highly dispersed polypyrrole on reduced graphite oxide for dopamine detection," *Biosensors and Bioelectronics*, Vol. 50, 157–160, 2013.

[94] Weaver, C. L., H. Li, X. Luo, and X. T. Cui, "A graphene oxide/conducting polymer nanocomposite for electrochemical dopamine detection: Origin of improved sensitivity and specificity," *Journal of Materials Chemistry B*, Vol. 2, No. 32, 5209–5219, 2014.

[95] Wang, W., G. Xu, X. T. Cui, G. Sheng, and X. Luo, "Enhanced catalytic and dopamine sensing properties of electrochemically reduced conducting polymer nanocomposite doped with pure graphene oxide," *Biosensors and Bioelectronics*, Vol. 58, 153–156, 2014.

[96] Mir, T. A., M. H. Akhtar, N. G. Gurudatt, J.-I. Kim, C. S. Choi, and Y.-B. Shim, "An amperometric nanobiosensor for the selective detection of K+-induced dopamine released from living cells," *Biosensors and Bioelectronics*, Vol. 68, 421–428, 2015.

[97] Mao, H., J. Liang, H. Zhang, Q. Pei, D. Liu, S. Wu, Y. Zhang, and X.-M. Song, "Poly(ionic liquids) functionalized polypyrrole/graphene oxide nanosheets for electrochemical sensor to detect dopamine in the presence of ascorbic acid," *Biosensors and Bioelectronics*, Vol. 70, 289–298, 2015.

[98] Arulraj, A. D., A. Arunkumar, M. Vijayan, K. B. Viswanath, and V. S. Vasantha, "A simple route to develop highly porous nano polypyrrole/reduced graphene oxide composite film for selective determination of dopamine," *Electrochimica Acta*, Vol. 206, 77–85, 2016.

[99] Taylor, I. M., E. M. Robbins, K. A. Catt, P. A. Cody, C. L. Happe, and X. T. Cui, "Enhanced dopamine detection sensitivity by pedot/graphene oxide coating on in vivo carbon fiber electrodes," *Biosensors and Bioelectronics*, Vol. 89, 400–410, 2017.

[100] Chen, J.-L., X.-P. Yan, K. Meng, and S.-F. Wang, "Graphene oxide based photoinduced charge transfer label-free near-infrared fluorescent biosensor for dopamine," *Analytical Chemistry*, Vol. 83, No. 22, 8787–8793, 2011.

[101] Yan, Y., Q. Liu, K. Wang, L. Jiang, X. Yang, J. Qian, X. Dong, and B. Qiu, "Enhanced peroxydisulfate electrochemiluminescence for dopamine biosensing based on au nanoparticle decorated reduced graphene oxide," *Analyst*, Vol. 138, No. 23, 7101–7106, 2013.

[102] Luo, Y., L. Ma, X. Zhang, A. Liang, and Z. Jiang, "SERS detection of dopamine using label-free acridine red as molecular probe in reduced graphene oxide/silver nanotriangle sol substrate," *Nanoscale Research Letters*, Vol. 10, No. 1, 230, 2015.

[103] Dutta, S., C. Ray, S. Mallick, S. Sarkar, R. Sahoo, Y. Negishi, and T. Pal, "A gel-based approach to design hierarchical cus decorated reduced graphene oxide nanosheets for enhanced peroxidase-like activity leading to colorimetric detection of dopamine," *The Journal of Physical Chemistry C*, Vol. 119, No. 41, 23 790–23 800, 2015.

[104] Kamali, K. Z., A. Pandikumar, G. Sivaraman, H. N. Lim, S. P. Wren, T. Sun, and N. M. Huang, "Silver@graphene oxide nanocomposite-based optical sensor platform for biomolecules," *RSC Advances*, Vol. 5, No. 23, 17 809–17 816, 2015.

[105] Guiard, B. P. and G. Gotti, "The high-precision liquid chromatography with electrochemical detection (HPLC-ECD) for monoamines neurotransmitters and their metabolites: A review," *Molecules*, Vol. 29, No. 2, 496, 2024.

[106] Nichkova, M., P. M. Wynveen, D. T. Marc, H. Huisman, and G. H. Kellermann, "Validation of an elisa for urinary dopamine: Applications in monitoring treatment of dopamine-related disorders," *Journal of Neurochemistry*, Vol. 125, No. 5, 724–735, 2013.

[107] Shinde, M. and G. Slaughter, "Advanced nanocomposite-based electrochemical sensor for ultra-sensitive dopamine detection in physiological fluids," *Frontiers in Lab on A Chip Technologies*, Vol. 4, 1549365, 2025.

[108] Ankitha, M., N. Shabana, A. M. Arjun, P. Muhsin, and P. A. Rasheed, "Ultrasensitive electrochemical detection of dopamine from human serum samples by Nb_2CT_x-MoS_2 hetero structures," *Microchemical Journal*, Vol. 187, 108424, 2023.

[109] Jabbari, S., B. Dabirmanesh, S. Daneshjou, and K. Khajeh, "The potential of a novel enzyme-based surface plasmon resonance biosensor for direct detection of dopamine," *Scientific Reports*, Vol. 14, No. 1, 14303, 2024.

[110] Fattinger, C., "Focal molography: Coherent microscopic detection of biomolecular interaction," *Physical Review X*, Vol. 4, No. 3, 031024, 2014.